Warsaw University of Technology

FACULTY OF PHYSICS

Master's diploma thesis

in the field of study Applied Physics

and specialisation Nuclear Physics and Technology

Femtoscopic correlations of pairs of nonidentical particles in Monte Carlo simulations for the CBM experiment

Wioletta Borzym

student record book number 284472

thesis supervisor
Prof. Dr Paolo Giubellino

thesis supervisor from Warsaw University of Technology
Prof. Dr Hanna Zbroszczyk

WARSAW 2022

Streszczenie

Tytuł pracy: Korelacje femtoskopowych par cząstek nieidentycznych wyznaczone w symulacjach modeli Monte Carlo na potrzeby eksperymentu CBM

Celem badań było uzyskanie informacji o funkcjach korelacyjnych par cząstek nieidentycznych w symulacjach Monte Carlo dla eksperymentu Compressed Baryonic Matter w placówce FAIR. Eksperyment CBM jest nadal w fazie przygotowań, a jego uruchomienie szacowane jest na 2025 rok. Do tego czasu można przygotować się, wykonując szereg zadań związanych z symulacjami procesu zderzeń ciężkich jonów, które mają odzwierciedlać przyszłe dane eksperymentalne.

Pierwszy paragraf pracy zawiera wprowadzenie w tematykę cząstek i oddziaływań fundamentalnych. Opisany jest Model Standardowy i diagram fazowy QCD. Omówiono też ideę badania zderzeń ciężkich jonów.

Zostało przedstawione zastosowanie metody femtoskopii do analizy danych zebranych ze zderzeń ciężkich jonów. Przedstawiono rodzaje dwucząstkowych funkcji korelacyjnych-korelacji par cząstek identycznych i korelacji par cząstek nieidentycznych. Istnieją trzy główne źródła korelacji femtoskopowych, z których niektóre mają silny lub niewielki wpływ na kształt funkcji korelacyjnych, w zależności od rodzaju analizowanych cząstek. Analiza funkcji korelacyjnych par cząstek nieidentycznych pozwala na zbadanie asymetrii czasowo-przestrzennej w procesie emisji.

W kolejnym rozdziale przedstawiony jest eksperyment Compressed Byronic Matter (CBM). Zilustrowano i opisano placówkę FAIR, budowę detektoru oraz opisy poddetektorów w eksperymencie CBM. Głównym celem eksperymentu jest zbadanie bardzo obiecującego obszaru diagramu fazowego QCD, który odpowiada materii przy bardzo wysokich gęstościach barionowych.

Kolejny rozdział skupia się na oprogramowaniu użytym do przeprowadzania potrzebnych analiz. Zawiera krótkie opisy modelu UrQMD wykorzystywanego do symulacji relatywistycznych zderzeń ciężkich jonów, oprogramowań ROOT i CBMROOT, które są głównymi narzędziami używanymi w CBM. Pokazano również schemat i kolejne etapy łańcucha symulacji-analizy w eksperymencie. Do ostatecznej analizy wykorzystano oprogramowanie NicaFemto.

Ostatnia część tej pracy zawiera uzyskane wyniki oraz ich omówienie. Przedstawione zostały analizy prowadzące do ustalenia granic p_T oraz y w zakresie których rozpatrywane były cząstki p, $\overline{p}$, κ^+, κ^-, π^+ oraz π^- w kolejnych analizach. Zaprezentowane zostały

też rozkłady podstawowych parametrów wykorzystywanych do opisu zarejestrowanych cząstek, tj. rozkłady czterowektoru położeń, czterowektoru pędu, pędu poprzecznego oraz promienia poprzecznego, a także rozkłady pospieszności i pseudopospieszności. Następnie omówiony został proces wyznaczania promienia źródła, ponieważ dane z produkcji masowej nie zawierały tej informacji. Finalnie, przedstawiona została potrzebna statystyka do uzyskania funkcji korelacyjnych par cząstek nieidentycznych, na zadanym poziomie niepewności 10%, 5% oraz 1%. Potrzebne statystyki zostały oszacowane dwoma sposobami.

Finalnie, w ostatnim rozdziale pracy omówione zostały uzyskane wyniki oraz możliwe przyszłe kroki badań.

Słowa kluczowe: femtoskopia, zderzenia ciężkich jonów, korelacje par cząstek nieidentycznych, CBM, FAIR, GSI

(podpis opiekuna naukowego) (podpis dyplomanta)

Abstract

Title of the thesis: Femtoscopic correlations of pairs of nonidentical particles in Monte Carlo simulations for the CBM experiment

The aim of the study is to gain information about nonidentical particles pairs correlation functions in Monte Carlo simulations for the Compressed Baryonic Matter experiment at FAIR. The CBM experiment is currently under construction and it will be launched in 2025. Until then one can prepare for the launch by carrying a number of tasks related to Monte Carlo simulations of heavy ion collisions process, designed to be similar to the experimental data.

The first chapter of the thesis introduces the subject of fundamental particles and interactions. It describes the Standard Model and QCD phase diagram. The idea of studying heavy-ion collisions is discussed.

The idea for femtoscopy method used for analyzing data collected from heavy ion collisions has been raised. The types of two-particle correlation functions - identical particles pairs correlation and nonidentical particles pairs correlation, have been outlined. There are three main sources of femtoscopic correlations, some of which have strong or little impact on the shape of the correlation functions, depending on the types of analysed particles. The analyses of nonidentcial particles pairs correlation functions allows to determine space-time asymmetry in the emission process.

In the next chapter, the Compressed Baryonic Matter (CBM) experiment is presented. The Facility for Antiproton and Ion Research and the detector setup for CBM experiment are illustrated and described. The main goal of CBM experiment is to study very promising part of the QCD phase diagram, which corresponds to the QCD matter at very high baryon densities.

The following section focuses on the software used to carrying out needed analysis. It contains the short descriptions of UrQMD model used to simulate relativistic heavy-ion collisions, ROOT and CBMROOT which are the main framework used in the CBM. The scheme of Simulation-Analysis chain in CBM has been shown. For the final analysis the NicaFemto framework was used.

The last part of this thesis contains obtained results and discussion about outcomes of the studies. The determination of the p_T and y cuts for the p, $\overline{p}$, κ^+, κ^-, π^+ and π^- particles, used in later analysis was shown. The distributions of the basic parameters used to describe the particles are also presented, i.e. the distributions of the position four-vector,

the momentum four-vector, the transverse momentum and the transverse radius, as well as the distributions of rapidity and pseudorapidity. Then the process of establishing the source radius is discussed as the mass production data do not contain this information. At last, the necessary statistics to obtain the correlation functions of pairs of non-identical particles at a given uncertainty level of 10%, 5% and 1% were presented. The statistics needed were estimated by two methods.

Finally, the final chapter of the thesis contains the discussion of the obtained results and possible future research steps.

Keyworlds: femtoscopy, heavy ion collision, nonidentical particle pairs correlations, CBM, FAIR, GSI

(podpis opiekuna naukowego) (podpis dyplomanta)

Politechnika Warszawska

Wioletta Borzym
284472
Fizyka Techniczna

Oświadczenie

Świadoma odpowiedzialności karnej za składanie fałszywych zeznań oświadczam, że niniejsza praca dyplomowa została napisana przeze mnie samodzielnie, pod opieką kierującego pracą dyplomową.
Jednocześnie oświadczam, że:

- niniejsza pracz dyplomowa nie narusza praw autorskich w rozumieniu ustawy z dnia 4 lutego 1994 roku o prawie autorskim i prawach pokrewnych (Dz.U. z 2006r. Nr 90, poz. 631 z późn. zm.) oraz dóbr osobistych chronionych prawem cywilnym.
- niniejsza praca dyplomowa nie zawiera danych i informacji, które uzyskałam w sposób niedozwolony,
- niniejsza praca dyplomowa nie była wcześniej podstawą żadnej innej urzędowej procedury związanej z nadawaniem dyplomów lub tytułów zawodowych,
- wszystkie informacje umieszczone w niniejszej pracy, uzyskane ze źródeł pisanych i elektronicznych, zostały udokumentowane w wykazie literatury odpowiednimi odnośnikami,
- znam regulacje prawne Politechniki Warszawskiej w sprawie zarządzania prawami autorskimi i prawa pokrewnymi, prawami własności przemysłowej oraz zasadami komercjalizacji.

Oświadczam, że treść pracy dyplomowej w wersji drukowanej, treść pracy dyplomowej zawartej na nośniku elektronicznym (płycie kompaktowej) oraz treść pracy dyplomowej w module APD systemu USOS są identyczne.

Warszawa, dnia (podpis dyplomanta)

Oświadczenie o udzieleniu Uczelni licencji do pracy

Politechnika Warszawska

Wioletta Borzym
284472
Fizyka Techniczna

Oświadczam, że zachowując moje prawa autorskie udzielam Politechnice Warszawskiej nieograniczonej w czasie, nieodpłatnej licencji wyłącznej do korzystania z przedstawionej dokumentacji pracy dyplomowej w zakresie jej publicznego udostępniania i rozpowszechniania w wersji drukowanej i elektronicznej[1]

Warszawa, dnia (podpis dyplomanta)

[1]Na podstawie Ustawy z dnia 27 lipca 2005 r. Prawo o szkolnictwie wyższym (Dz.U. 2005 nr 164 poz. 1365) Art. 239. oraz Ustawy z dnia 4 lutego 1994 r. o prawie autorskim i prawach pokrewnych (Dz.U. z 2000 r. Nr 80, poz. 904, z późn. zm.) Art. 15a. "Uczelni w rozumieniu przepisów o szkolnictwie wyższym przysługuje pierwszeństwo w opublikowaniu pracy dyplomowej studenta. Jeżeli uczelnia nie opublikowała pracy dyplomowej w ciągu 6 miesięcy od jej obrony, student, który ją przygotował, może ją opublikować, chyba że praca dyplomowa jest częścią utworu zbiorowego."

Contents

1. Introduction

Heavy ion collision experiments collecting data at energies of a few GeV per nucleon-nucleon pair are designed to study selected areas of the phase diagram of quantum chromodynamics. These are a complex physical processes which involve, for example, the production of particles.

The Compressed Baryonic Matter (CBM) experiment, which is currently under construction at Facility for Antyproton and Ion Research in Darmstadt, Germany, will be able to perform systematic measurements of particles produced in the heavy-ion collisions. Thanks to especially high interaction rates of up to 10 MHz the comprehensive study of matter in the region of high baryon densities is possible. This includes, for example, the study of the equation of state of nuclear matter at neutron star core densities.

Although the launch of the CBM experiment is planned for 2025, until then, in preparation of the future work on the experimental data, a number of tasks related to Monte Carlo simulations of the heavy ion collision process, that will take place during the experiment, are being carried out.

By using the method of femtoscopy the properties of the source can be examined, which cannot be obtained by any other experimental technique. This involves the analysis of information about the momentum of emitted particles. Traditional method of femtoscopy is based on determining the correlation function of two particles.

Femtoscopic two-particle correlations for many years have provided information on the time-space evolution of a source produced by heavy ion collisions. The two-particle correlations are most often investigated as a function of their momentum difference, where the aim is to estimate the size of the emission source of the considered types of particles.

However, two-particle correlations can also be determined as a function of other variables, which allows a closer look at the production process of the studied pairs of

particles. Correlations of nonidentical particles indicate a space-time asymmetry in the emission process, as heavier particles are emitted earlier or closer to the edge of the source.

Originally, the aim of the thesis was to obtain the correlation functions for non-identical particle pairs, but due to the insufficient sample of data produced in mass production, which passed the reconstruction stage, other analyzes were performed that will help in the future analysis of the reconstructed data.

2. Physical introduction

2.1 Standard model

The Standard Model (SM) [1] of particles and their interactions is a model proposed by scientists in the 1970s which describes the basic components of matter and interactions between them. The Standard Model classifies the elementary particles, strong, electromagnetic and weak interactions. Also, it outlines theories such as: quantum chromodynamics, quantum mechanics and electroweak interactions.

2.1.1 Particles

According to the Standard Model all matter is built from fermions and bosons.
Fermions are the particles with half-integer spin. They are described by Fermi-Dirac statistics, so the Pauli Exclusion Principle, which states that no two identical fermions can be in the same quantum state, must be obeyed by them. We can distinguish two types of fermions: quarks and leptons.

We can distinguish six types (flavours) of quarks within the three generations. The 1^{st} generation of quarks contains: (u) up quark and (d) down quark, the 2^{nd} generation contains: (c) charm quark and (s) strange quark and the 3^{rd} generation contains:
(t) top quark and (b) bottom quark. Quarks have their correspondent anti-particles called anti-quarks.

As was said before, fermions are described by Fermi-Dirac statistics, so they must obey the Pauli Exclusion Principle. To explain why there are identical quarks in the same particle, e.g. one (u) up and two (d) down quarks in neutron, an additional degree of freedom called *colour* was introduced. There are three colours: *red*, *green* and *blue* with three correspondent anti-colours: *anti-red (cyan)*, *anti-green (magenta)* and *anti-blue (yellow)*. Those names are symbolical and they are not related to any visual trait of the quark.

There are also six lepton types within the three generations. The 1^{st} generation of leptons contains: (e) electron and (υ_e) electron neutrino, the 2^{nd} generation of leptons contains: (μ) muon and (υ_μ) muon neutrino and the 3^{rd} generation of leptons contains: (τ) tau and (υ_τ) tau neutrino. The electrons, muons and taus have an electric charge, while their neutrinos are hard to examine due to the lack of the electric charge. Electrons are stable particles, while muons and taons decay spontaneously.

The spin of bosons is described by integers. They are described by Bose-Einstein statistics. There are six known bosons: (g) gluon, which is the carrier of the strong interactions, (γ) photon, which is the carrier of the electromagnetic force, W^+, W^- and Z^0 bosons, which are the carriers of the weak interaction and the Higgs boson (H), which is the carrier of the Higgs field. The mass of the particles depends on the strength of its interaction with the Higgs field.

The Fig.2.1 shows all particles considered by the Standard Model.

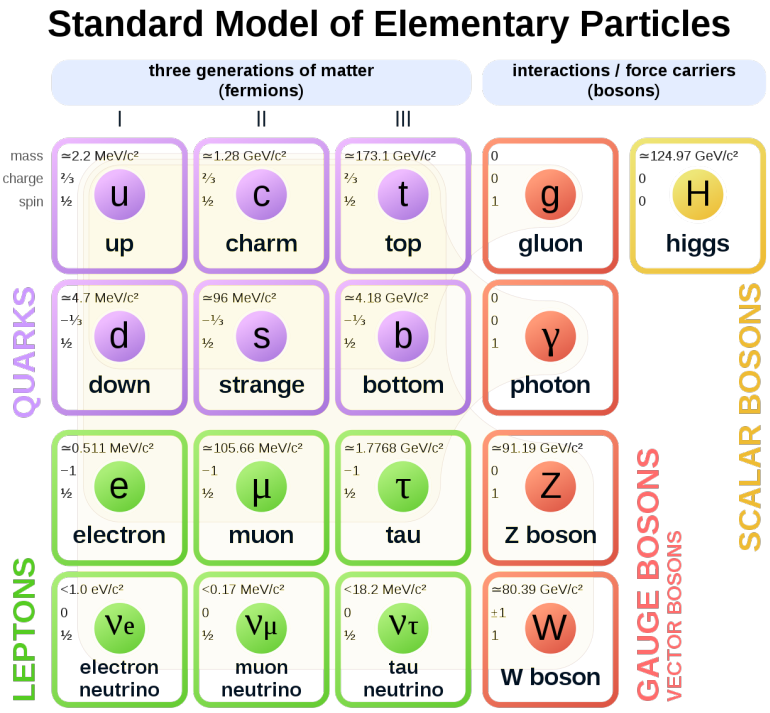

Figure 2.1: Elementary particles in Standard Model [2]

Leptons can exist as a free particles, while quarks are bounded inside the particle. Quarks are bonded into different combinations of *colourless* particles, which are:

- Baryons - contain three quarks with different colours.
- Anti-baryons - contain three quarks with different anti-colours.
- Mesons - contain a quark with an anti-quark with corresponding anti-colour.

2.1.2 Fundamental Interactions

Standard Model describes three out of four fundamental interactions between particles. Gravity is the only one, which is not described by the SM.

Those four types of fundamental interactions are:

- *Strong* - responsible for bounding quarks into hadrons and nuclei, the carrier of the interaction are gluons.
- *Electromagnetic* - long-range force, which only acts between charged particles, the carrier of this interaction are photons.
- *Weak* - enables quark and leptons to exchange energy and mass, the carrier of the interaction are the W^+, W^-, Z^0 bosons.
- *Gravitational* - long-range force, describes interactions between massive objects, the carrier of this interaction are gravitons.

The main information about the interactions are shown in Table 2.1.

Table 2.1: Fundamental interactions.

Interaction	Particles experiencing	Carrier	Range
Strong	quarks and gluons	gluons	short range
Electromagnetic	electrically charged particles	photon γ	infinite
Weak	quarks and leptons	W^+, W^-, Z^0	short range
Gravitational	all particles	gravitons	infinite

2.1.3 Physics beyond Standard Model

The Standard Model is so far the most reasonable description of the elementary particles and interactions. However, it still has a few limitations, such as:

- There are 19 parameters, that cannot be proven theoretically.
- It does not include gravitational interaction, despite the fact that it is the dominating interaction in the universe.
- It does not include the dark matter and the dark energy.
- There is no explanation of 3 generations of quarks and leptons.
- There is no explanation of the asymmetry between matter and antimatter.

2.2 Quantum Chromodynamics

Quantum Chromodynamics [3] is a theory describing the strong interactions. It focuses on the quarks and gluons and their behaviour under different conditions. It states that quarks cannot exist as single particles. So, the additional quantum number called *colour* was

introduced. Quarks are bonded into different combinations and form *colourless* particles, which are baryons, anti-baryons and mesons. While at extremely high temperatures or high enough densities of hadronic matter, quarks and gluons are liberated from their bond and start to behave like free particles.

2.2.1 The QCD potential

The bond between quark and anti-quark in QCD is described by potential V expressed by the formula:

$$V = -\frac{4}{3}\frac{\alpha_s}{r} + kr \tag{2.1}$$

where:
r - distance between quarks,
α_s - coupling constant,
k - elasticity coupling constant

Fig.2.2 shows the QCD potential V as a function of distance.

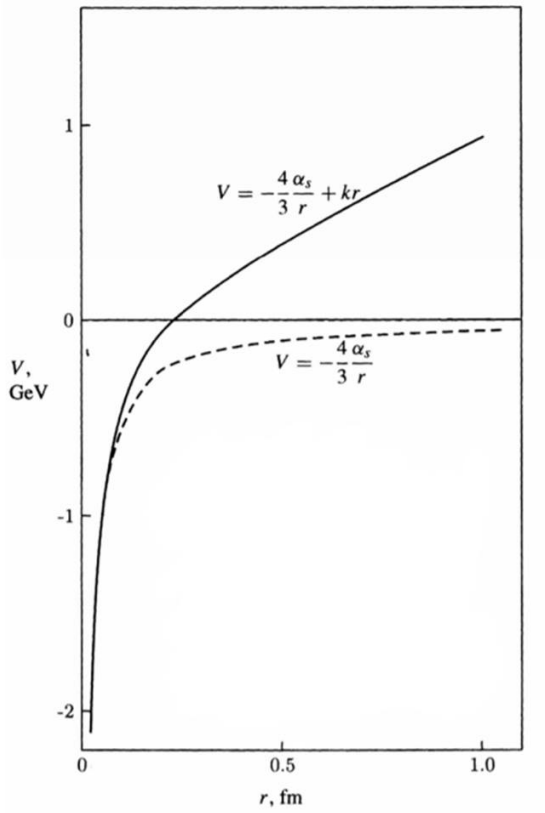

Figure 2.2: The QCD potential. [4]

As the Standard Model states, quarks cannot exist as single particles. They are bonded inside the hadrons and cannot separated. According to the equation 2.1, the QCD potential V increases with the distance between the quarks. An increase in the potential V value to the limit value, causes a creation of a new quark - anti-quark pair. This creation of the new pair is more energy sufficient than sustaining the existing bound between quarks in the old pair.

2.2.2 The QCD phase diagram

As was mentioned previously quarks cannot exist as single particles. Under ordinary conditions, the state of matter, where quarks and gluons are bounded into hadrons, is called the Hadron Gas state.

Nevertheless, at high enough temperature or energy densities, one can obtain the state of matter, where quarks and gluons are liberated from their bonds and behave like a free particles. This state is called Quark-Gluon Plasma (QGP).

Fig.2.3 shows a scheme of the QCD phase diagram. To describe the state of matter, two variables are used: temperature T and net baryon density μ_B, as they can both express other quantities, e.g. energy density, pressure, entropy.

Temperature T is a measure of a particles' mean kinematic energy. The net baryon density μ_B is related to the the imbalance between the number of baryons and antibaryons.

The QCD phase diagram [5] shows two states of the matter: Hadronic Gas and Quark-Gluon Plasma and phase transitions between those two states.

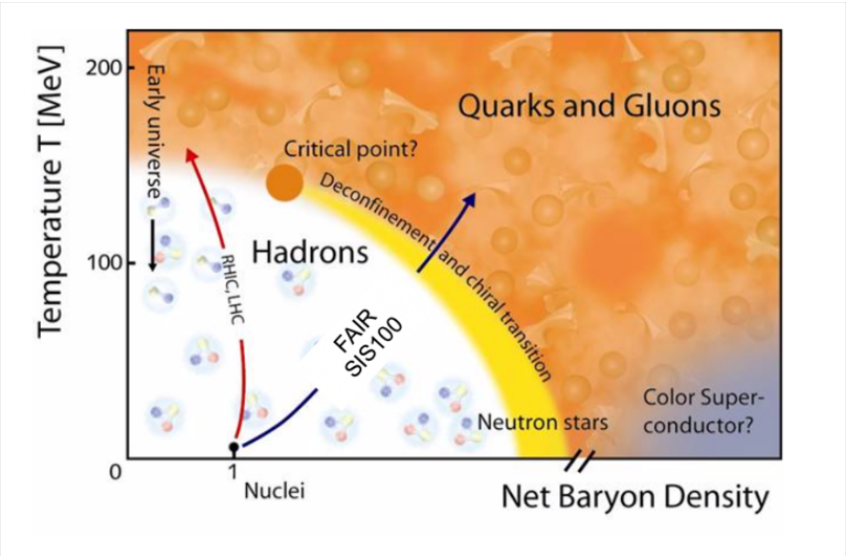

Figure 2.3: The QCD phase diagram. [6]

To distinguish the type of transition, which occurs when matter change the state, the Gibbs free energy is used and it is defined as:

$$G(p,T) = U + pV - TS \tag{2.2}$$

where:
U - initial energy,
V - volume,
T - temperature
S - entropy

There are transition areas between the Hadron Gas and Quark-Gluon Plasma, which are:

- 1^{st} *order transition*, where Gibbs free energy is continuous but the 1^{st} and 2^{nd} derivatives are not. On the Fig.2.3 1^{st} order transition is marked as yellow area located after Critical Point.
- 2^{nd} *order transition*, possibly for the Critical Point separating cross-over and 1^{st} order transitions, where Gibbs free energy and 1^{st} derivative are both continuous but 2^{nd} derivative is not. On the Fig.2.3 2^{nd} order transition is marked as an orange point.
- *Cross-over transition* , where there is a rapid change in the parameters of the physical system. On the Fig.2.3 cross-over transition occurs before the Critical point, for low net Baryon Densities.

Exploration of the QCD phase diagram in different regions is possible by studying heavy-ion collisions. Heavy-ion collisions also enables to study the topic of QGP state of the matter, which cannot be observed directly, because of its short lifetime. By analysing the particles which originated from colliding nuclei we can study and explore the QGP state of matter.

2.3 Heavy-Ion Collisions

Exploration of the QCD phase diagram in different regions is possible by studying heavy-ion collisions. Heavy-ion collisions also enable to study the topic of QGP state of the matter, which cannot be observed directly, because of its short lifetime.

One can recreate the state of QGP in the laboratory and explore it by analysing the particles which originated from heavy-ion collisions.

Some experiments, e.g. STAR and ALICE work in the collider mode (two beams are aimed at each-other and made to collide), while different experiments, e.g. CBM and HADES work in the fixed target mode (the particle beam is aimed at a stationary target).

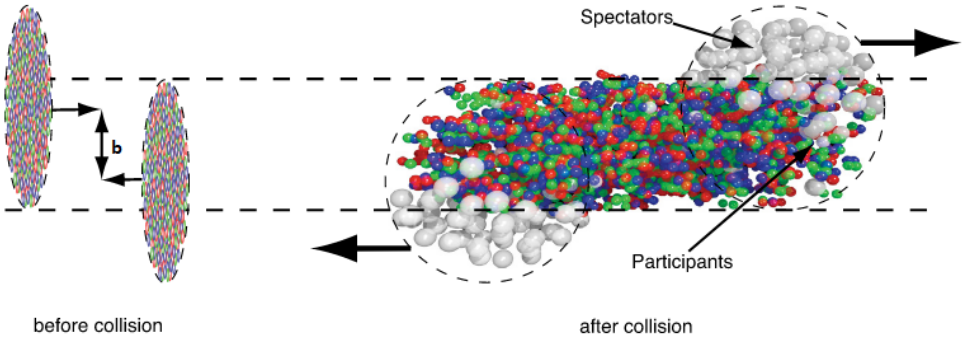

Figure 2.4: Geometry of heavy-ion collision.[7]

Fig.2.4 shows a scheme of collision of two nuclei. It also shows the two types of nuclei, which can be distinguish during the heavy-ion collision:

- participants - nucleons taking part in the collision by interacting with other nucleons,
- spectators - nucleons which do not react with other particles and therefore not taking part in the collision.

Fig.2.5 shows the stages of space-time evolution of the heavy-ion collision.
Those stages are [8]:

1. *Preequilibrium state*, where quarks and gluons are produced and start to interact with each-other, creation of the fireball.
2. Creation of *Quark-Gluon Plasma (QGP)*.
3. *Mixed phase*, between QGP and Hadron gas state.
4. *Hadronization*, where quarks and gluons form into hadrons.

5. *Chemical and thermal freeze-out*:
   - Chemical freeze-out, during which formation of the chemical composition of particles is finished. Estimated temperature of this phenomenon is of order of $T \sim 150 - 170MeV$.
   - Thermal freeze-out (also called *kinematic freeze-out*), where the exchange of momenta between particles has stopped. Estimated temperature of this state is of order of $T \sim 90 - 130MeV$.

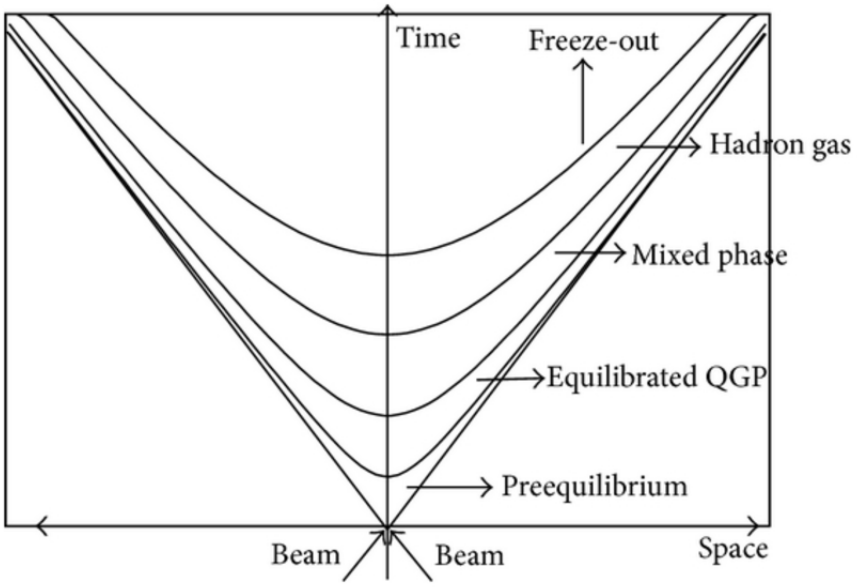

Figure 2.5: The space-time evolution of heavy-ion collision. [9]

2.3.1 Kinematic variables used in High Energy Physics

In the analysis of data gained as a result of the heavy-ion collisions there are some most important variables used to describe each particle. The most important one is the four-momentum vector $[p_x, p_y, p_z, E]$, where p_x, p_y, p_z are momentum projections on the x, y and z axis and E is the energy of the particle. Besides that, in data gained from simulations, there is also information about the four-position vector $[x, y, z, t]$, describing the positions of freeze-out and impact parameter b, which describes the centrality of the collision. Impact parameter was shown in Fig.2.6. Impact parameter, marked as b is equal to the shortest length of the vector connecting the centers of mass of two colliding ions just in the moment of their overlap. If the value of b is higher than the radius of ion, then the collision is called peripheral. As the value of impact parameter b declines, and it is smaller than the value of ion's radius, centrality of collision increases.

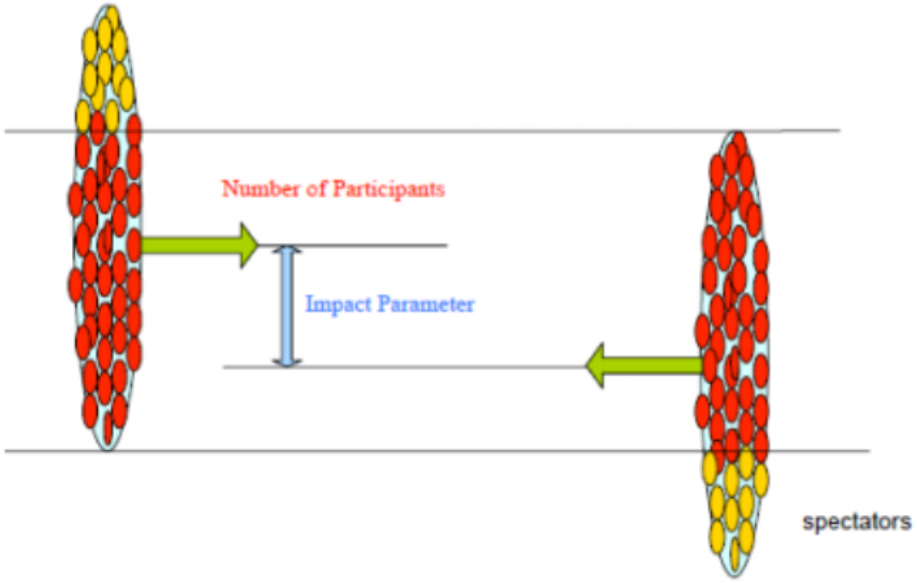

Figure 2.6: A scheme of two colliding nuclei, where the impact parameter and two types of nuclei during the heavy-ion collision: participants and spectators, are explained. [10]

The other important variables used to describe heavy-ion collisions are:

- ϕ - an angle between the direction of particle's motion and the reaction plane
- total momentum of a particle:

$$p = \sqrt{p_x^2 + p_y^2 + p_z^2} \tag{2.3}$$

- transverse momentum - the momentum perpendicular to the beam axis:

$$p_T = \sqrt{p_x^2 + p_y^2} \tag{2.4}$$

- longitudinal momentum - the momentum parallel to the beam axis:

$$p_L = p_z \tag{2.5}$$

- rapidity - the equivalent to velocity (Lorentz invariant):

$$y = \frac{1}{2} \ln \frac{E + p_L}{E - p_L} \tag{2.6}$$

- pseudorapidity (used when the energy of the collision is very high), where θ is an angle

between beam axis and three-momentum vector (Fig.2.7):

$$\eta = -\ln \tan \frac{\theta}{2} \tag{2.7}$$

- transverse radius:

$$r_T = \sqrt{x^2 + y^2} \tag{2.8}$$

- mean transverse momentum of 2 particles k_T:

$$k_T = \frac{|p_{T1} + p_{T2}|}{2} \tag{2.9}$$

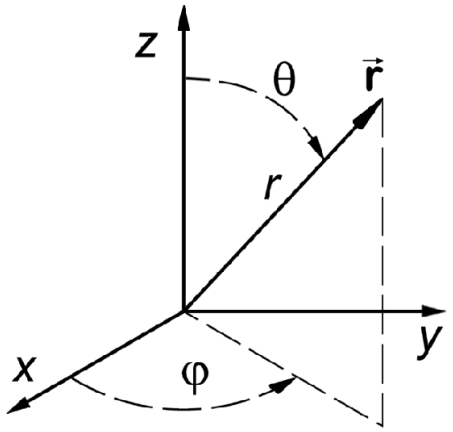

Figure 2.7: Explanation of ϕ and θ angles in the kinematic coordinates. [11]

3. Femtoscopy

Femtoscopy [3] allows us to study properties of objects of sizes at the level of one femtometer ($10^{-15}m$) and lifetimes of order of $10^{-23}s$, which cannot be obtained in any direct method.

Traditional method of femtoscopy is based on determining the two-particle correlation functions. This involves study of difference in particles momenta.

The idea of two-particle correlation function is shown in Fig.3.1. It presents two particles (1 and 2) being emitted from the source S, from positions $\vec{r}_1$ and $\vec{r}_2$, with momenta, respectively, $\vec{p}_1$ and $\vec{p}_2$.

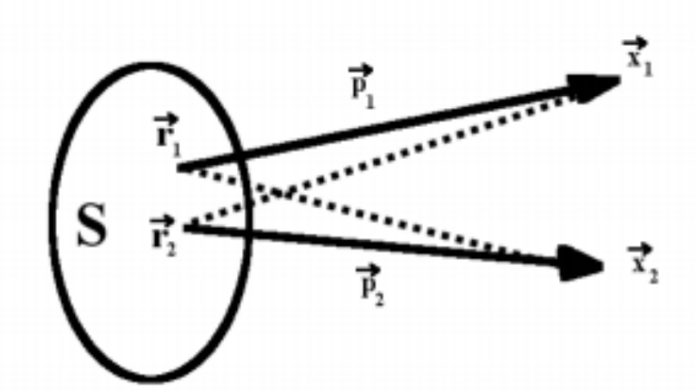

Figure 3.1: The idea of two-particle correlation function, where two particles (1 and 2) are being emitted from the source S, from positions $\vec{r}_1$ and $\vec{r}_2$, with momenta, respectively, $\vec{p}_1$ and $\vec{p}_2$.[12]

It is possible to register the 1 particle in the emission point $\vec{x}_2$ and the 2 particle in the emission point $\vec{x}_1$. This case is shown in Fig.3.1 as dashed lines. [12]

3.1 Construction of the theoretical and experimental correlation function

The two-particle correlation function is defined as the probability of finding two particles at the same place and time divided by the probability of finding the first and the second particles separately. It is traditionally defined as:

$$\vec{C}(\vec{p_1},\vec{p_2}) = \frac{P_2(\vec{p_1},\vec{p_2})}{P_1(\vec{p_1})P_1(\vec{p_2})} \tag{3.1}$$

where:
$\vec{p_1}$ and $\vec{p_2}$ are particles momenta,
$P_2(\vec{p_1},\vec{p_2})$ is the probability of finding two particles at the same place and time,
$P_1(\vec{p1})$,$P_1(\vec{p_2})$ are the probabilities of finding two particles separately.

If one takes info consideration two identical bosons, their wave functions are expressed by formula 3.2.

$$\psi(x_1,x_2) = \frac{1}{\sqrt{2}}[e^{i(p_1x_1+p_2x_2)} + e^{i(p_1x_2+p_2x_1)}] \tag{3.2}$$

The probability of emission of each particle is then expressed by:

$$S(\vec{x},\vec{p}) = f(\vec{x})g(\vec{p}) \tag{3.3}$$

where, $f(\vec{x})$ is a spatial emission distribution, and $g(\vec{p})$ is momentum emission distribution.

Then, one-particle distribution is defined as:

$$P_1(p) = \int S(x,p)dx \tag{3.4}$$

And the two-particle distribution is expressed by:

$$P_2(p_1,p_2) = \int\int S(x_1,p_1)S(x_2,p_2)|\psi(x_1,x_2)|^2dx_1dx_2 \tag{3.5}$$

In case of the pair of identical fermions the correlation function takes the form of:

$$C_2(\vec{p_1},\vec{p_2}) = \frac{1}{4}[1+cos(\vec{q}\vec{x})] + \frac{3}{4}[1-cos(\vec{q}\vec{x})] = 1 - \frac{1}{2}[cos(\vec{q}\vec{x})] \tag{3.6}$$

, where $\vec{q} = \vec{p_1} - \vec{p_2}$ and $\vec{x} = \vec{x_1} - \vec{x_2}$.

In the experiment, the correlation function is described as the distribution of differences in momenta ($\vec{q} = \vec{p_1} - \vec{p_2}$) of particles coming from the same event $A(\vec{q})$, which is also called *signal*, divided by the distribution of differences in momenta of particles coming from different events $B(\vec{q})$, which is also called *background*.

The formula for two-particle correlation function is defined by function 3.7.

$$C(\vec{q}) = \frac{A(\vec{q})}{B(\vec{q})} \tag{3.7}$$

3.2 The coordinates system and parameterization of the correlation function

In the technique of femtoscopy, there are two main coordinate systems: Longitudinal Co-Moving System (LCMS) and Pair Rest Frame (PRF).

In the LCMS frame, the correlation function is described as a function of Q_{inv}, which is described as:

$$Q_{inv} = |\vec{p_1} - \vec{p_2}| = \sqrt{(\vec{p_1} - \vec{p_2})^2 + (E_1 - E_2)^2} \tag{3.8}$$

where p_1 and p_2 are particles momenta and E_1 and E_2 are particles energies.

The scheme of the Q_{inv} is also shown in Fig.3.2.

The LCMS coordinate system is generally used while studying identical particle pairs.

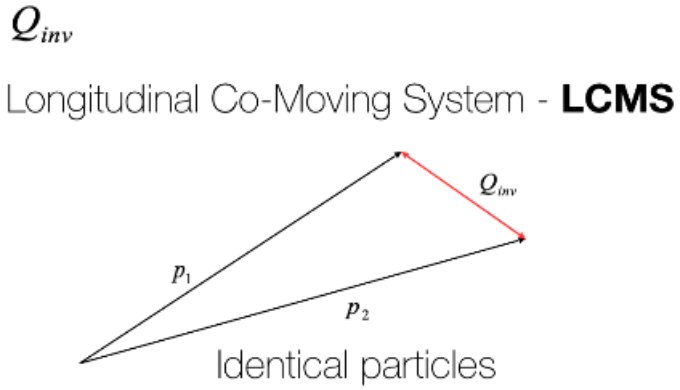

Figure 3.2: The definition of Q_{inv} in the LMCS coordinate system. [6]

In the LCMS coordinate system, there are three main dimensions, which are also shown in the Fig.3.3:

- *long* - parallel to the direction of the beam,

- *out* - parallel to the total pair momentum in a transverse plane,
- *side* - perpendicular to the *long* and *out* directions

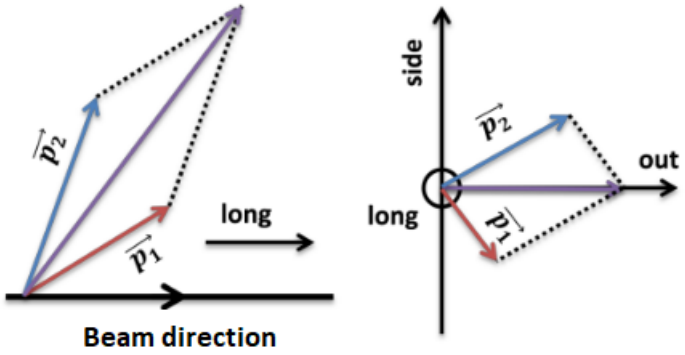

Figure 3.3: $Long$, out and $side$ directions. [13]

In the Pair Rest Frame coordinate system, the two-particle correlation function is analyzed in terms of k^*, which is defined as:

$$\frac{1}{2}Q_{inv} = \vec{k^*} = \vec{p_1} = -\vec{p_2} \tag{3.9}$$

In the PRF system, momenta of particles compensate each other and the total momentum of two particles is equal to 0. Fig.3.4 shows the scheme of PRF system and $k*$.

The Pair Rest Frame coordinate system is generally used while studying nonidentical particle pairs.

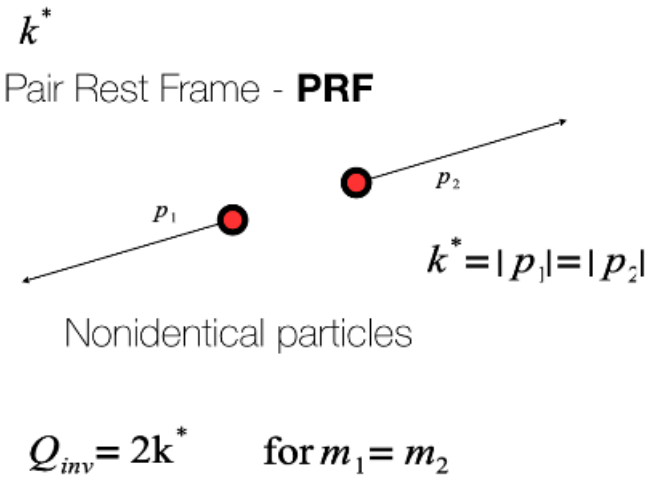

Figure 3.4: Pair Rest Frame coordinate system with explanation of k^*. [6]

The parametrization of the two-particle correlation function (in case of two identical bosons) is done to study the size of the source (Fig.3.5), the shape of it and also to gain information about the dynamics of the source at freeze-out stage.

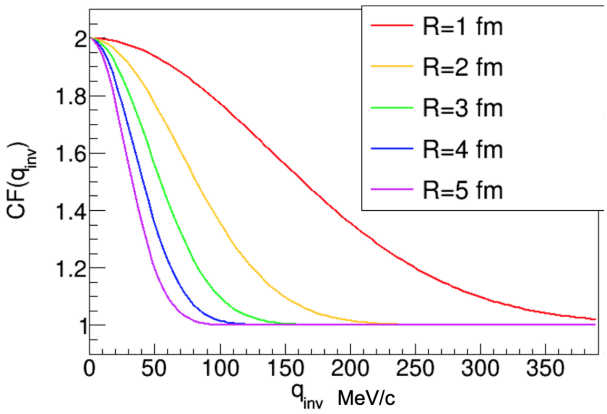

Figure 3.5: The dependence of the shape of a function and the size of the source, which can be established by studying correlation function. [14]

The correlation function takes form of a 1-D analytical function, if taking into account only Quantum Statistics effects, and is described as:

$$C(\vec{q}) = 1 + \lambda e^{-Q_{inv}^2 R_{inv}^2} \tag{3.10}$$

where R_{inv} is the radius of the source and λ is a parameter characterizing the incoherence of the source.

In the LCMS frame the 3D parametrization is used and it takes form of:

$$C(\vec{q}) = 1 + \lambda e^{-Q_{long}^2 R_{long}^2 - Q_{out}^2 R_{out}^2 - Q_{side}^2 R_{side}^2} \tag{3.11}$$

where R_{long}, R_{out} and R_{side} are the radius of the source in directions of long, out and side.

3.3 Types of correlation functions

While studying correlation functions we can distinguish two types of two-particle correlations, which can also influence the shape of a correlation function:

- correlation functions of identical particle pairs, e.g. $\pi^+\pi^+$ or pp correlations,
- correlation functions of nonidentical particle pairs, e.g. $\pi^+\pi^-$ or $\pi^-\kappa^+$ correlations.

The two main sources of femtoscopic correlations are:

- **Quantum Statistics (QS)** - can only be observed for identical particle pairs and depending on the type of particles it can be described by:

- The Bose-Einstein statistics for bosons, where the probability of finding two particles in the same quantum state is high and it results in positive correlation,.
- The Fermi-Dirac statistics for fermions, where because of the Pauli exclusion principle, two particles cannot be found in the same quantum state and it results in negative correlation.

• **Final State Interaction (FSI)**

- **Coulomb Interaction (COUL)** - depends on the charge of particles. If two particles are like-sign they repulse each other and we observe negative interactions. If two particles are unlike-sign they attract each other and we observe positive interactions.
- **Strong Interaction (SI)** - short range interaction, which has an important impact on the shape of correlation function for baryons and negligibly small impact on the shape of correlation function for other types of particles.

3.3.1 Identical particles correlation

In case of identical particles correlation, the shape of the function is strongly influenced by Quantum Statistics for bosons and by Final State Interactions for fermions.

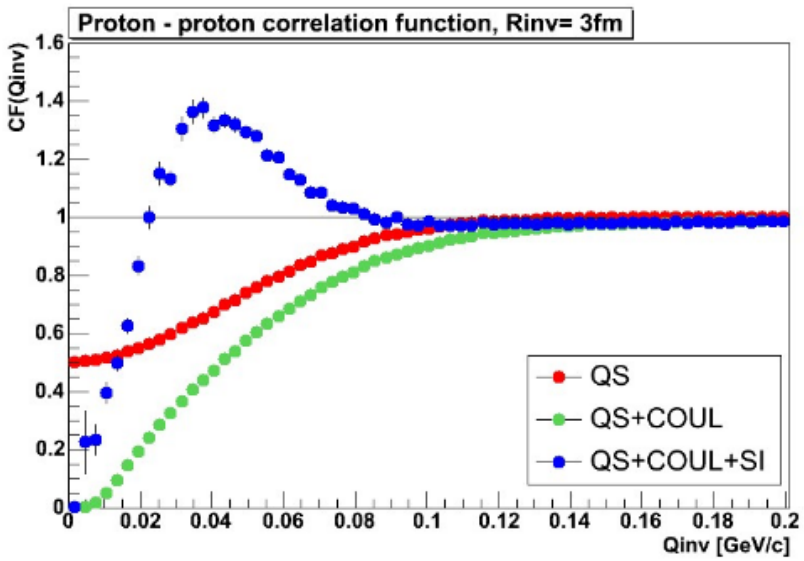

Figure 3.6: The correlation functions for pp, showing the impact of interactions on the shape of the function. [15]

The Fig.3.6 shows the pp correlation functions, influenced by different sets of interactions: QS, QS+COUL and QS+COUL+SI.

3.3.2 Nonidentical particles correlation

The correlation function of nonidentical particles are strongly influenced by Final State Interactions.

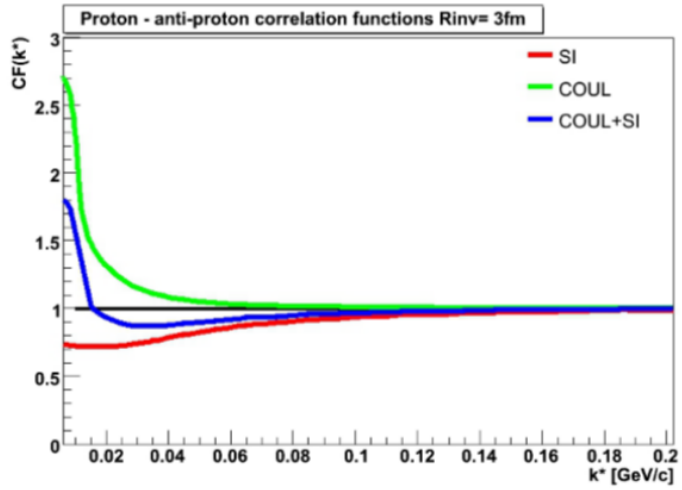

Figure 3.7: The correlation functions for $p\overline{p}$, showing the impact of interactions on the shape of the function. [15]

The Fig.3.7 shows the $p\overline{p}$ correlation functions, influenced by different sets of interactions: SI, COUL and COUL+SI.

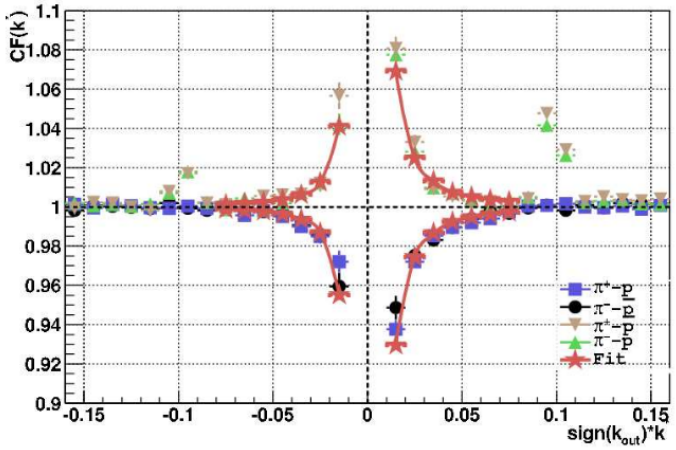

Figure 3.8: The correlation functions for $\pi\kappa$, showing the impact of Coulomb Interaction, depending on the charges of π and κ. [16]

If two particles are like-signed the Coulomb Interaction is negative and the correlation function takes negative values, while if two particles are unlike-sign the Coulomb Interaction

is positive and correlation function takes positive values.

The Fig.3.8 shows the $\pi\kappa$ correlation functions for different sets of charged particles. The $\pi^+\kappa^+$ and $\pi^-\kappa^-$ correlation functions show negative Coulomb Interaction, while the $\pi^+\kappa^-$ and $\pi^-\kappa^+$ correlation functions show positive Coulomb Interaction.

In studies of nonidentical two-particle correlations the Pair Rest Frame (PRF) system is used. The correlation functions of nonidentical particle pairs are measured versus the $k*$.

3.4 Asymmetry in nonidentical particles correlations

Nonidentical two-particle correlation functions allow to study the size of the emitting source and additionally the emission asymmetries between two particles with different mass. Those asymmetries are closely related to the collective behaviour of matter.

The ability to study the relative emission shifts is used to study the time ordering of the emission of various particles. [16]

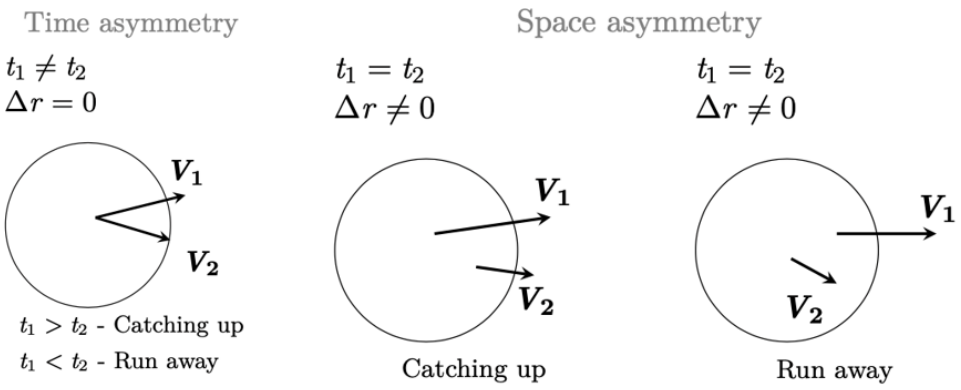

Figure 3.9: A scheme of time asymmetry and space asymmetry in emission of particles. Two scenarios are shown - Catching up pair and Run away pair. [17]

The Fig.3.9 shows the two scenarios of particle pairs - Catching up and Run away particle pairs.

Catching up particle pair scenario describes the situation, where the first particle is emitted from the center of the source with given velocity v_1 and the second particle is emitted closer to the edge of the source with given velocity v_2, which is higher than v_1. In this case, time of interaction between particles is longer and correlation is stronger.

Run away particle pair scenario describes the situation, where the first particle is emitted closer to the edge of the source with given velocity v_1 and the second particle is emitted from the center of the source with given velocity v_2, which is lower than v_1. In this case, time

of interaction between particles is shorter and correlation is weaker.

The non-identical correlation function is represented as a set of two histograms - one for $C+$ and one for C. This allows for the determination of the source size and a study of the Double Ratio to access asymmetries. [16]

The $C+$ function is obtained for Catching up particle pairs and the $C-$ function is obtained for Run away particle pairs. By dividing $C+$ by $C-$ one can create a function called Double Ratio. Double Ratio allows the study of asymmetries.

Fig. 3.10 shows examples of Double Ratio for like-sign particle and unlike-sign particle pairs.

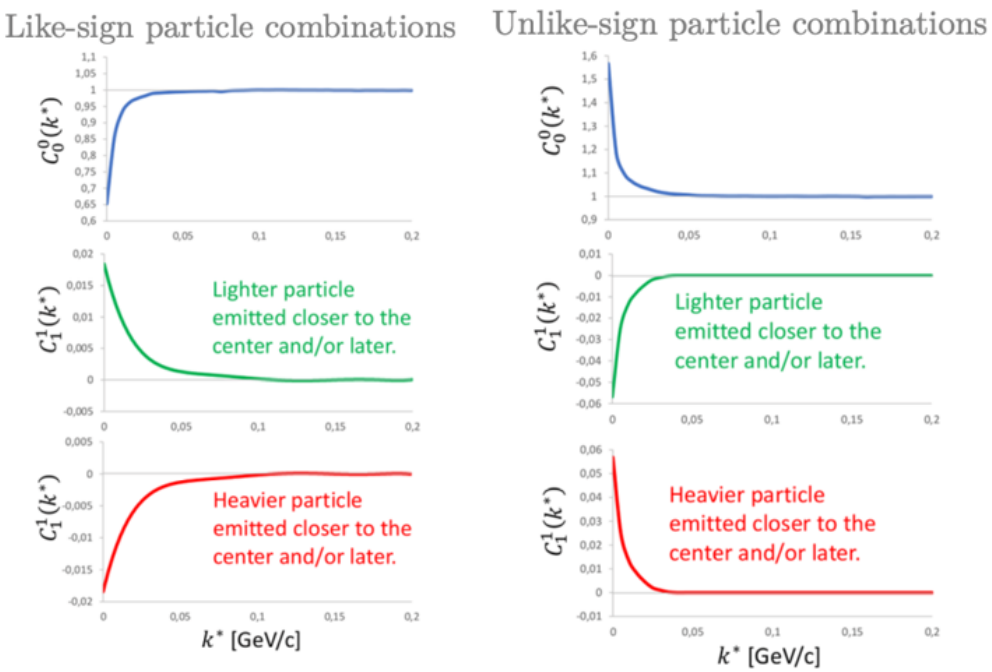

Figure 3.10: Examples of Double Ratio functions for like-sign particle pairs and unlike-sign particle pairs. [17]

For the like-sign particle pair, e.g. $\pi^+\kappa^+$, when the Double Ratio function shows values larger than unity, one can tell that the lighter particle is emitted closer to the center of the source and/or later. When the Double Ratio function for the like-sign particle pair takes values lower than unity, one can tell that the heavier particle is emitted closer to the center of the source and/or later.

For the unlike-sign particle pair, e.g. $\pi^-\kappa^+$, when the Double Ratio function shows values lower than unity, one can tell that the lighter particle is emitted closer to the center of the source and/or later. When the Double Ratio function for the unlike-sign particle pair takes values higher than unity, one can tell that the heavier particle is emitted closer to the center of the source and/or later.

4. The CBM Experiment

4.1 Facility for Antiproton and Ion Research

The Facility for Antiproton and Ion Research (FAIR) is situated in Darmstadt, Germany. It is an expansion of the GSI Helmholz Centre for Heavy Ion Research. Fig.4.1 shows the structure of the facility, where the existing parts are shown in grey and blue, while the red objects are under construction. FAIR will consist of 8 ring accelerators, 2 linear accelerators and about $3,5km$ of the beam pipes.

It comprises the SIS100 synchrotron with rigidity of $100Tm$. SIS100 is going to be the main circular synchrotron, run in a fix-target mode.

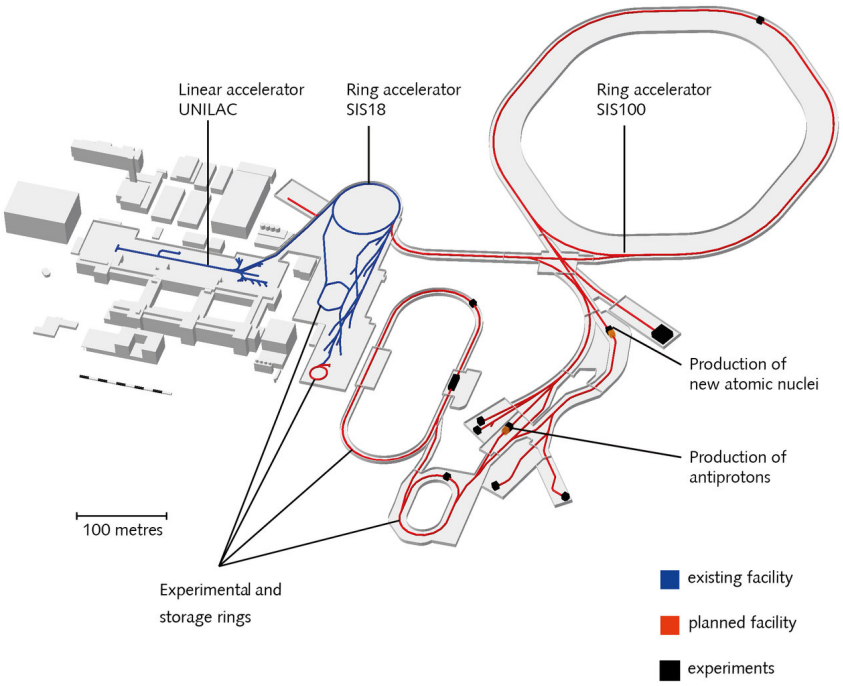

Figure 4.1: Layout of Facility for Antiproton and Ion Research. [18]

In the first stages the SIS100 accelerator will provide heavy-ion beams with energies up

to $11AGeV$ for Au, $14AGeV$ for light ions like Ca and $29AGeV$ for protons.

The four pillars of FAIR are Compressed Baryonic Matter Experiment (CBM), NUclear STructure, Astrophysics and Rections Experiment (NUSTAR), antiProton ANnihilation at Darmstadt Experiment (PANDA) and Atomic, Plasma Physics and Applications (APPA). [19]

The CBM Experiment is still in the construction stage. The first data taking is planned for 2025.

4.2 The CBM physics goals and observable

The research program of the CBM experiment at FAIR focuses on the measurements of diagnostic probes of the early and dense phase of the fireball evolution. The experimental goal is to measure these rare diagnostic probes with very high precision in spite of low multiplicities (Predicted multiplicities for CBM Experiment are shown in Fig.4.2). In order to compensate that fact, the measurements will be performed at extremely high reaction rates going up to 10 MHz as shown in Fig.4.2, which require the development of detectors and data acquisition with extraordinary speed and precision. [18]

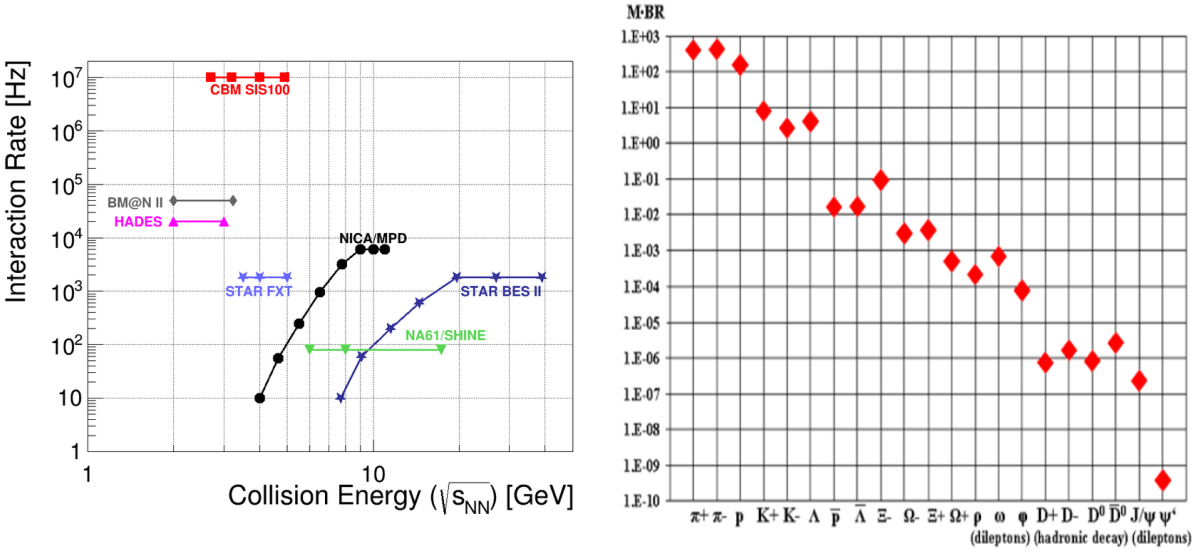

Figure 4.2: On the left side: comparison of interaction rates and center of mass collision energies of high energy experiments [18]. On the right side: Model predictions for yields (multiplicies) of probes intended to be measured by CBM. [18].

The main goal of the CBM is to explore the extraordinary region of the QCD phase diagram, which corresponds to the QCD matter at very high baryon densities. Such high baryon densities could be found i.e. in the neutron star core.

The CBM experiment is designed to study the QCD critical point, the phase transition

between hadronic and quark-gluon matter, the existence of exotic QCD phases and the exuation-of-state (EOS). EOS describe the state of matter by a given set of physical conditions.

4.3 CBM Detector Setup

The experimental setup of the CBM detector is shown in Fig. 4.3. It has two possible configurations: electron detection layout and muon detection system, which are shown in Fig. 4.3. The CBM experimental setup consists of a number of sub-detectors which are: the Silicon Tracking System (STS) and Micro-Vertex Detector (MVD) inside a dipole magnet for tracks reconstruction, Ring Imaging Cherenkov Detector (RICH) and Transition Radiation Detector (TRD) detectors for electron identification, a Time of Fight (TOF) detector for hadron identification, an Electromagnetic Calorimeter (ECAL) for the measurement of neutral probes, and a forward calorimeter Projectile Spectator Detector (PSD) for event characterisation in terms of centrality and reaction plane angle. The RICH detector can be replaced by the Muon Chamber System (MUCH) for measurements involving muons. [20]

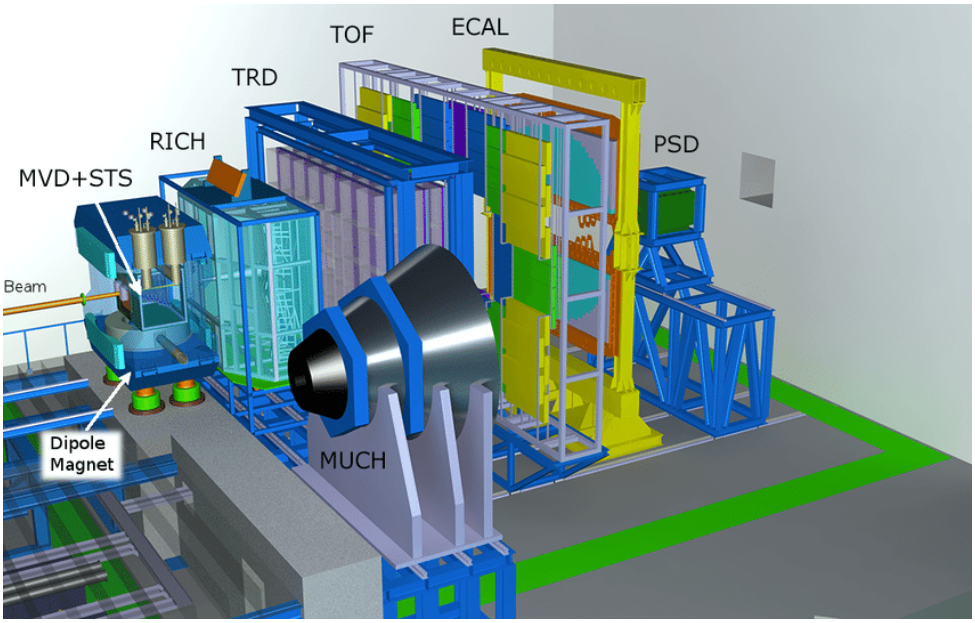

Figure 4.3: The CBM experimental detector setup. [21]

The Silicon Tracking System (STS) provides the information needed to reconstruct the track of any charged particle and determine its momentum. STS consists of 8 layers of double-sided silicon micro-strips sensors. The sensors are connected to the read-out electronics with ultra light micro-cables. The sub-detector is positioned 30 cm downstream from the target, inside the dipole magnet.

4.3. CBM DETECTOR SETUP

The Micro Vertex Detector (MVD) provides the means to determine the primary vertices of short lived particles. It consists of 4 layers placed 5, 10, 15 and 20cm downstream from the target, inside the dipole magnet.

The Ring Imagining Chereknov Detector (RICH) provides the identification of electrons and suppression of pions. RICH consists of focusing mirrors, photo detector planes and gas radiator. The detector is positioned 1,6m downstream from the target, outside the dipole magnet, behind the STS sub-detector in electron detection layout.

The Muon Chamber System (MUCH) detects muons by preforming a moment-dependent identification. MUCH consists of 5 layers of hadron absorbers and tracking detector planes between them. The first absorber panel is made of carbon plate (60cm thickness). It is followed by 4 iron panels (20, 20, 30 and 100cm thickness). This sub-detector is placed behind the STS sub-detector in muon detection layout, instead of the RICH sub-detector.

The Transition Radiation Detector (TRD) allows further particle tracking and identification of electrons and positrons. It consists of 1 layer. TRD is placed 5m downstream the target.

The Time of Flight (TOF) measures the velocity of the particles. Along with other detectors it allows to determine mass-to-charge ratio. It is placed about 6m downstream of the target.

The Electromagnetic Calorimeter (ECAL) measures the direct photons and other particles decaying into photons. It consists of 140 layers of lead (1mm thickness) and scintillator (1mm thickness).

The Projectile Spectator Detector (PSD) provides the collision centrality determination and the reaction plane extraction. It consists of 44 individual modules which are made of 60 lead-scintillator layers each. [21]

5. Software

Because of the fact that the CBM experiment is currently under construction, there is no experimental data to be studied yet. To prepare for the future analysis one can study data simulated to be as close as possible to the experimental data. This gives one a chance to provide verification of theories and realistic estimations of detector's response.

In high-energy physics, to simulate random high-energy collisions, Monte Carlo (MC) event generator tool is used. MC methods are crucial for computational physics and related fields. They consist of a few steps: designing, simulation and optimization, then data analysis is carried out and corrections are made, finally one can compare simulated data to the experimental one. The output of MC generator with detector simulations is data close to experimental one.

5.1 UrQMD model

Ultra-Relativistic Quantum Molecular Dynamic model (UrQMD) is a well established and integrated Monte Carlo simulation package used to simulate relativistic heavy-ion collisions. Fig. 5.1 shows a simulation of two heavy nuclei.

It has a large set of physics models that handle various interactions of particles in wide energy range. UrQMD has a number of applications in computational, particle and high-energy experimental physics. It was created using FORTRAN programming language.

In a single transport model, UrQMD enables to gain information and understanding in topics like creation of a dense hadronic matter, properties of nuclear matter, creation of mesonic matter and anti-matter, transport of rare probes in hadronic matter.

5.2 ROOT

ROOT is a framework, created at CERN, for processing and analysing high-energy physics data. As it is intended to process data from high-energy physics experiments, it is designed to work with high computing efficiency.

The data container in ROOT is called *tree*, which contains substructures of *branches*

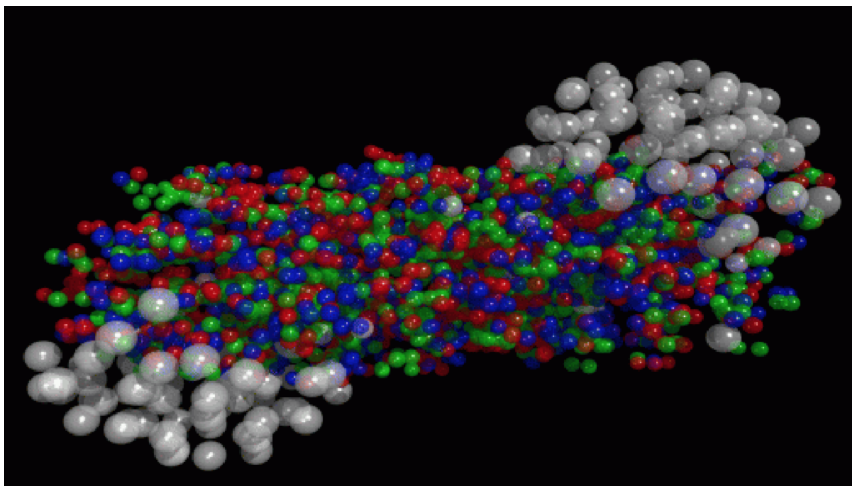

Figure 5.1: A scheme of the collision of two heavy nuclei. The white points are protons and neutrons, while red, blue and green ones are quarks. [22]

and *leaves*, where raw data is stored. Data from the following entries could be obtained by increasing the index in the *tree*. This type of storage allows to avoid memory allocation problems.

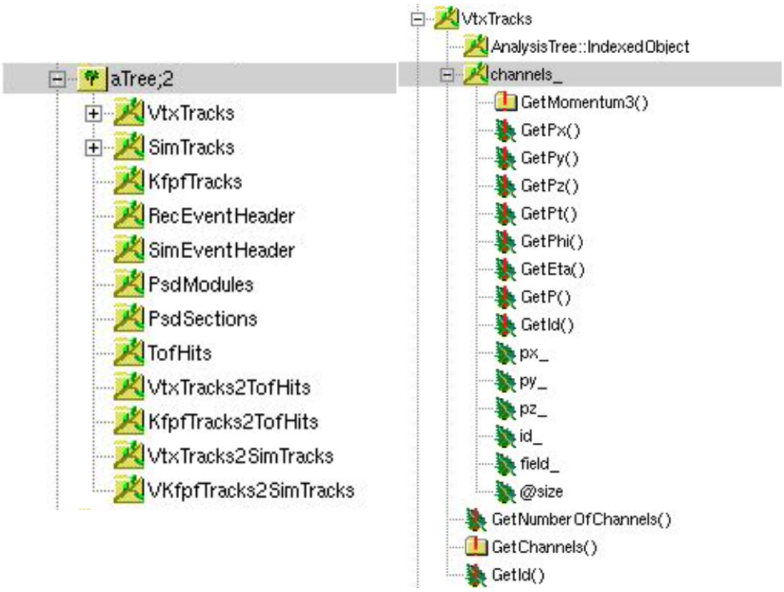

Figure 5.2: An example of ROOT *tree* with *branches* and *leaves* containing raw data from CBM data analysis.

5.3 Simulation process in CBM

CBMRoot is a framework created for the CBM experiment. It is based on ROOT system. It contains additional libraries, which enable user to perform the simulations of the CBM detector. Fig.5.3 shows a typical simulated collision event in the CBM detector system and an example of analysis which enables to study decay of Ω into daughter particles: Λ and κ^+ and then, the decay of Λ particle into p and π^-.

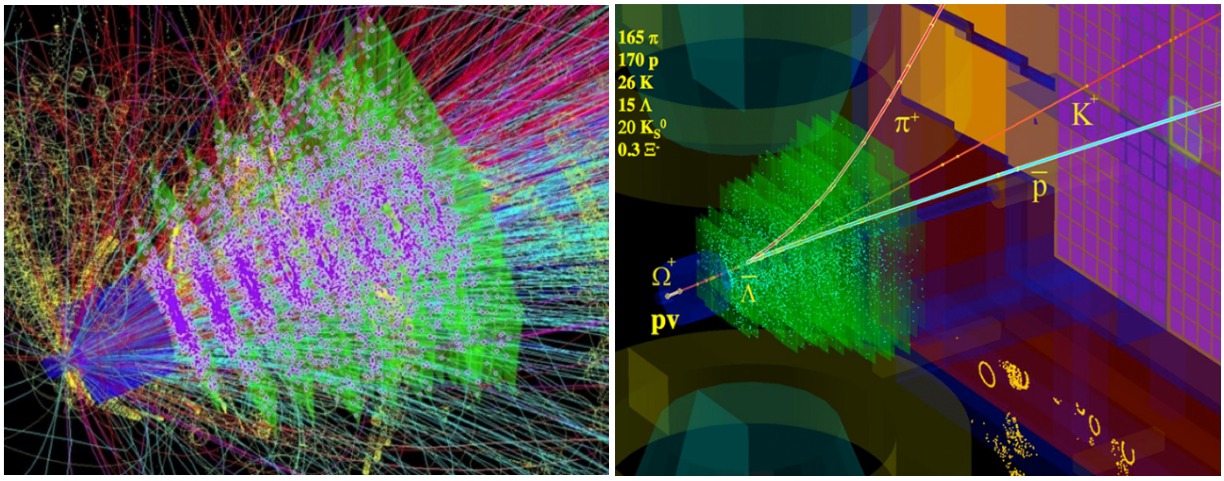

Figure 5.3: A typical collision event simulated in the CBM detector system (right) and an example of Ω decay into Λ and κ^+ particles and Λ decay into π^- and p particles in the CBM detector (left).[20]

The full Simulation-Analysis chain is shown in Fig.5.4. First 3 steps: Generation of Events, Transport and Digitization, are the simulation part of the process, while Hit Finder, Reconstruction and Physics Analysis are the analysis part. In the simulation, one takes the simulated collisions from MC simulator, determine particles properties at the target vertex, then transport particles through the detector and determine detector's response. In analysis process, the physical space points parameters are determined from detector hits. Then, momentum vectors and PID for all tracks are established. Finally, the data is ready for calculations and analysis.

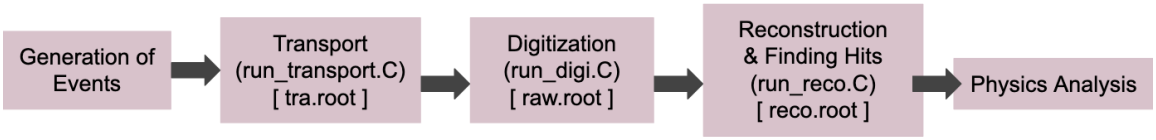

Figure 5.4: Simulation-Analysis process chain in CBM.

The process of simulation in CBM is done with use of a few data objects and tasks. The first object is MC Point (from MC data). It works as an input for a task of Merging (Transport

step of Simulation-Analysis process). After that, merged MC Points will work as an input of a task called Digitizer (Digitization step of Simulation-Analysis process). The output of Digitizer task is called Digit, which is an input for next task, Hit Finder (Finding Hits step of Simulation-Analysis process). Hit Finder task will produce data object called Hit. Finally, after the task of Reconstruction (Reconstruction step in of Simulation-Analysis chain) Track data object is obtained. Track can be now used to running needed physics analysis.

5.4 NicaFemto

NicaFemto [23] is a framework for HBT analysis with FairROOT based frameworks. It is a code developed by Dr. Daniel Wielanek for femtoscopy analysis in the MPD (NICA), however, the software can also be used for a simple flow or spectrum analysis in experiments that use the FairRoot framework as a base.[24]

A part of NicaFemto framework is still under optimization stage. In this thesis, methods for calculating correlation functions and fitting methods from NicaFemto are used, and it should be taken into consideration that they are still in the stage of improvement.

6. Results

6.1 Simulation Process

The first stage of the analysis carried out in this thesis was to simulate heavy-ion collisions by using the UrQMD model.

The following results will be performed for four beam momentum values: $12[AGeV/c]$, $7.95[AGeV/c]$, $4.4[AGeV/c]$ and $3.3[AGeV/c]$ and for two centrailities. Centrality in the CBM is described by impact parameter b. The central collisions $0-10\%$ are described by the impact parameter in range of $b \in (0;3.2)[fm]$ and non-central ones $10-100\%$ are described by the impact parameter in range of $b \in (3.2;15.0)[fm]$.

The first calculations consisted of estimation of the p_T and y ranges, in which the following analysis will be done. For that reason, distributions of $p_T(y)$ were created, for both data from UrQMD and from Monte Carlo data, which is the data with the simulation with the detector response, from the Common Production data. Common Production is data generated and reconstructed for the common use of the whole CBM collaboration. The distributions of $p_T(y)$ for MC data were shown in the Fig.6.1
Tab.6.1 shows established cuts for the p, $\overline{p}$, π^+, π^-, κ^+, κ^-, Λ and $\overline{\Lambda}$ particles from UrQMD data and Tab.6.2 shows established cuts for the p, $\overline{p}$, π^+, π^-, κ^+, κ^-, Λ and $\overline{\Lambda}$ particles from MC data from Common Production.

The next part of the basic analysis was to create the distributions of the most important variables used to describe heavy-ion collisions, such as the four-position vector of the particles $[x,y,z,t]$, the four-momentum vector $[p_x,p_y,p_z,E]$ and p_T, r_T, y, η. Distributions of those variables, for 100 000 $Au-Au$ central and non-central collisions, for $12[AGeV/c]$ beam momentum, are presented at histograms in Fig.6.2, Fig.6.3 and Fig.6.4 for central collisions and Fig.6.5, Fig.6.6 and Fig.6.7 for non-central collisions.

Table 6.1: Ranges of p_T and y used in further analysis, obtained from distributions of $p_T(y)$ for the p, $\overline{p}$, π^+, π^-, κ^+, κ^-, Λ and $\overline{\Lambda}$ particles from UrQMD data, where there is still information about freez-out.

particle	p_T range [GeV/c]	y range
p	(0.2 ; 2.0)	(-1.0 ; 1.0)
$\overline{p}$	(0.2 ; 2.0)	(-2.0 ; 2.0)
π^+	(0.2 ; 1.0)	(-2.0 ; 2.0)
π^-	(0.2 ; 1.0)	(-2.0 ; 2.0)
κ^+	(0.2 ; 1.5)	(-2.0 ; 2.0)
κ^-	(0.2 ; 1.5)	(-1.8 ; 1.8)
Λ	(0.2 ; 2.0)	(-1.5 ; 1.5)
$\overline{\Lambda}$	(0.2 ; 2.0)	(-1.5 ; 1.5)

Table 6.2: Ranges of p_T and y used in further analysis, obtained from distributions of $p_T(y)$ for the p, $\overline{p}$, π^+, π^-, κ^+, κ^-, Λ and $\overline{\Lambda}$ particles shown in Fig.6.1 from Monte Carlo data (Common Production).

particle	p_T range [GeV/c]	y range
p	(0 ; 1.0)	(-0.5 ; 3.5)
$\overline{p}$	(0.1 ; 2,0)	(-0.1 ; 3.2)
π^+	(0 ; 1.0)	(-1.0 ; 4.0)
π^-	(0 ; 1.0)	(-1.0 ; 4.0)
κ^+	(0 ; 1.5)	(-0.5 ; 3.5)
κ^-	(0 ; 1.5)	(-0.5 ; 3.5)
Λ	(0.1 ; 2.0)	(-0.2 ; 3.2)
$\overline{\Lambda}$	(0.1 ; 2.0)	(0 ; 3.2)

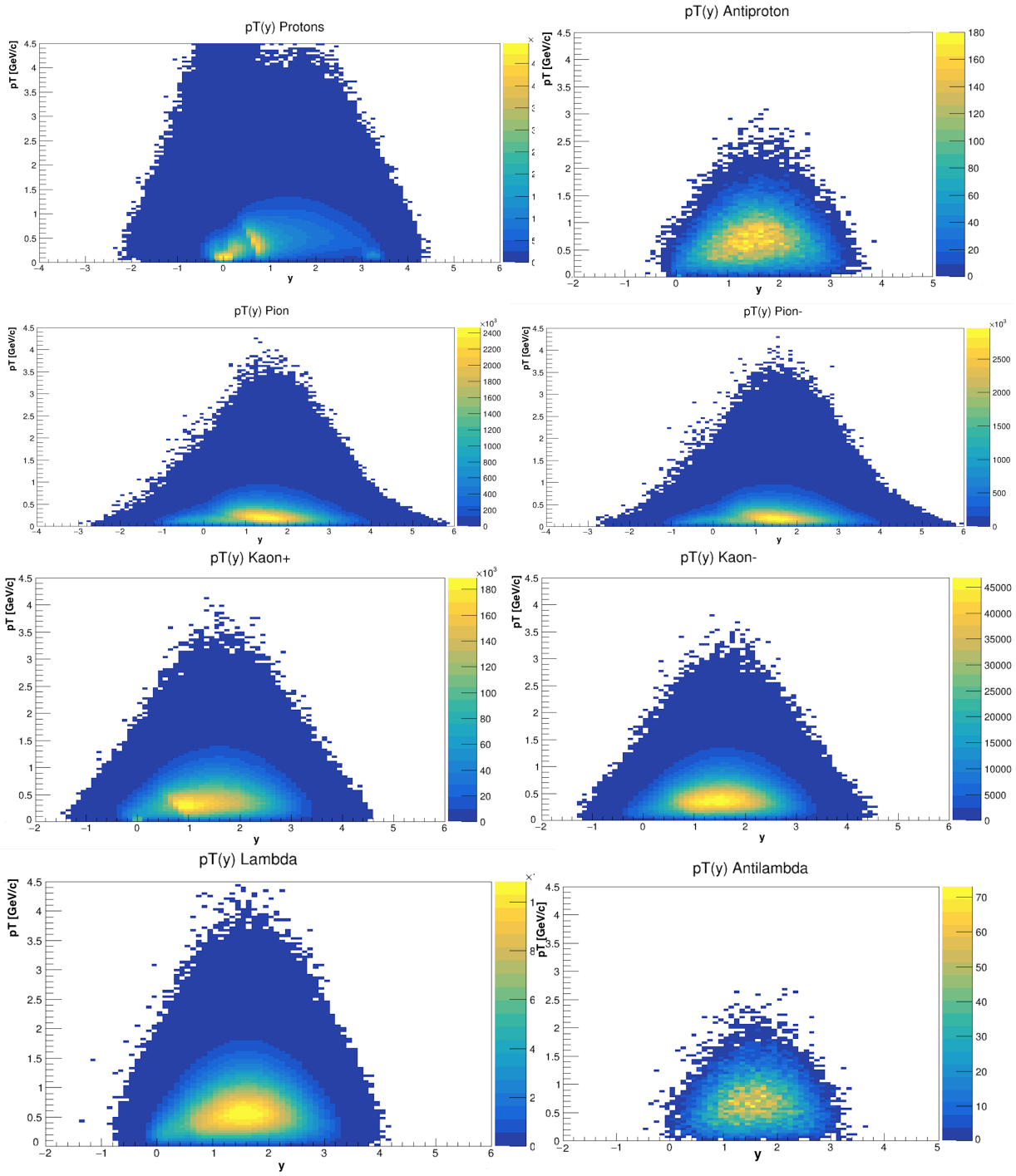

Figure 6.1: $p_T(y)$ distributions for p, $\overline{p}$, π^+, π^-, κ^+, κ^-, Λ and $\overline{\Lambda}$ from Monte Carlo data (Common Production).

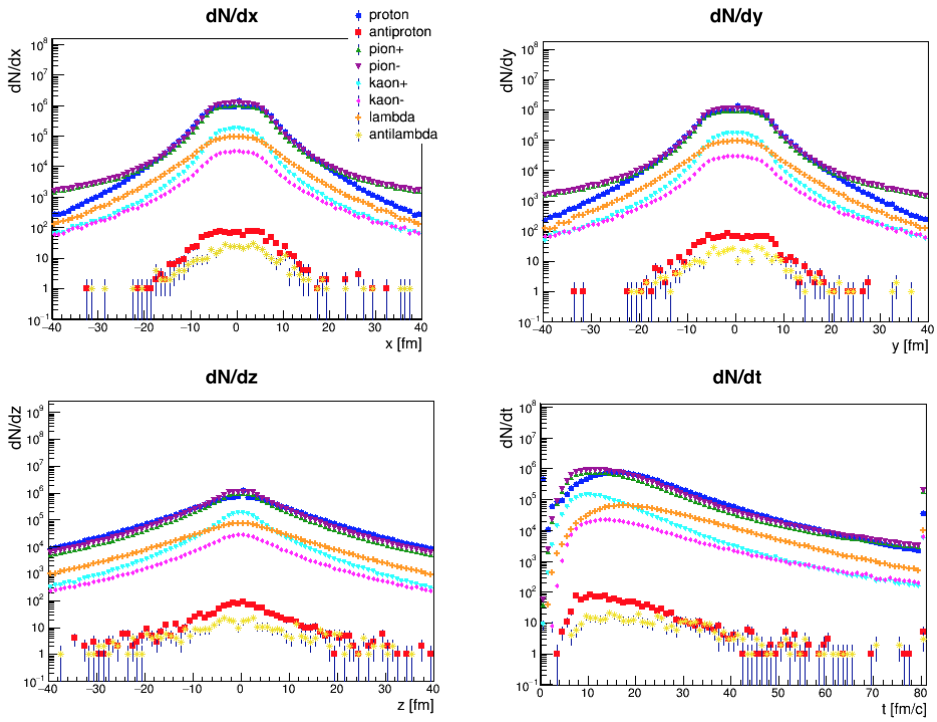

Figure 6.2: Distribution of four-position vector $[x, y, z, t]$ for p, $\overline{p}$, π^+, π^-, κ^+, κ^-, Λ and $\overline{\Lambda}$, for 100 000 Au-Au central collisions, for $12[AGeV/c]$ beam momentum.

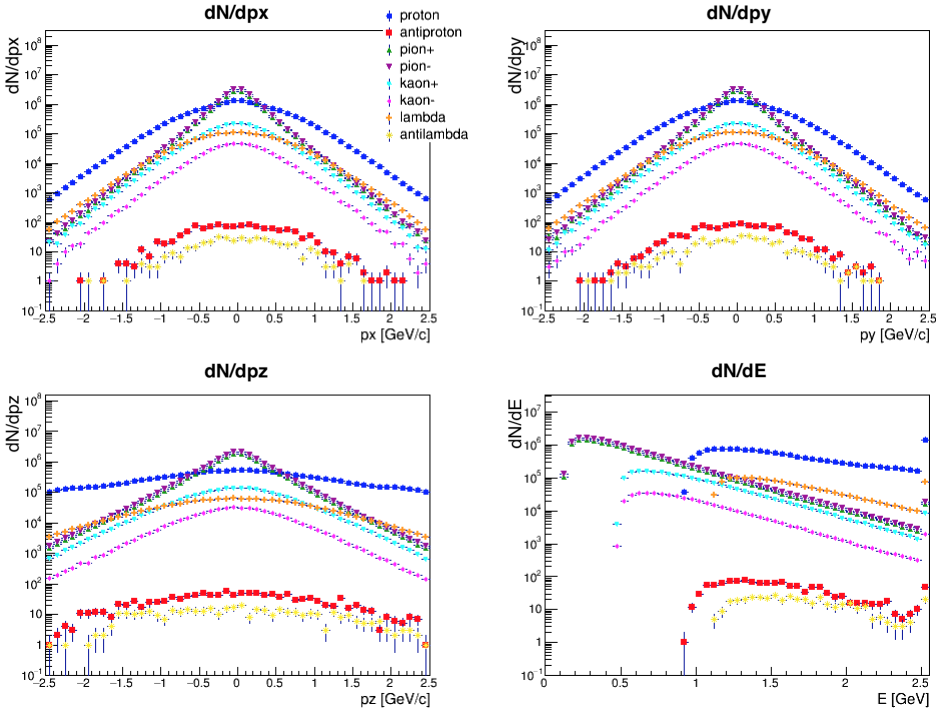

Figure 6.3: Distribution of four-position vector $[p_x, p_y, p_z, E]$ for p, $\overline{p}$, π^+, π^-, κ^+, κ^-, Λ and $\overline{\Lambda}$, for 100 000 Au-Au central collisions, for $12[AGeV/c]$ beam momentum.

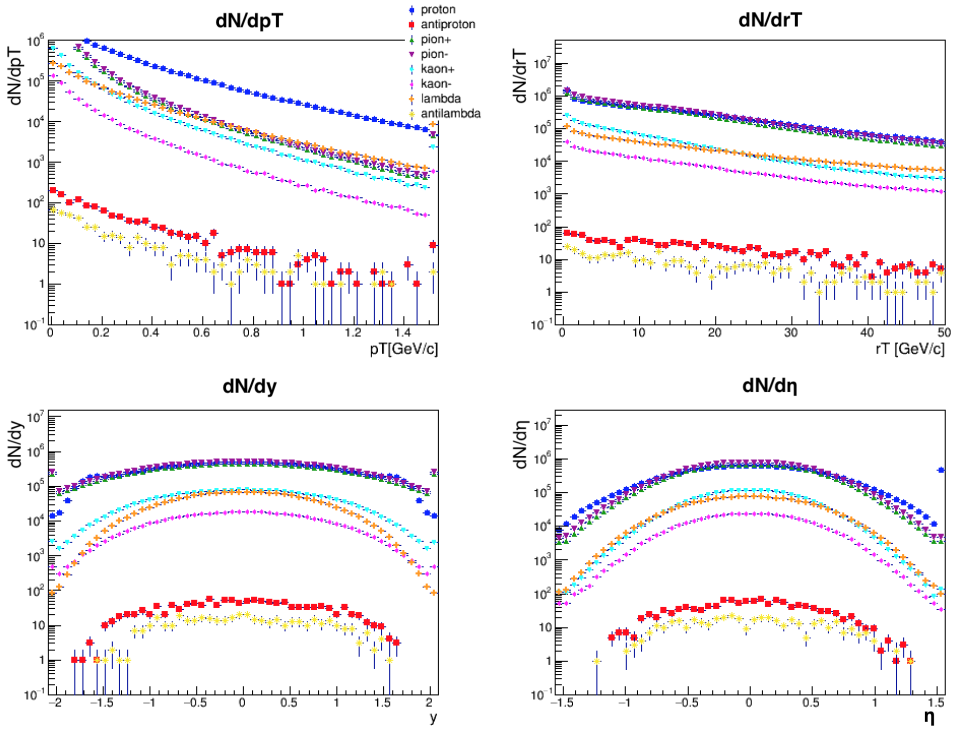

Figure 6.4: Distributions of p_T, r_T, y, η for p, $\overline{p}$, π^+, π^-, κ^+, κ^-, Λ and $\overline{\Lambda}$, for 100 000 Au-Au central collisions, for $12[AGeV/c]$ beam momentum.

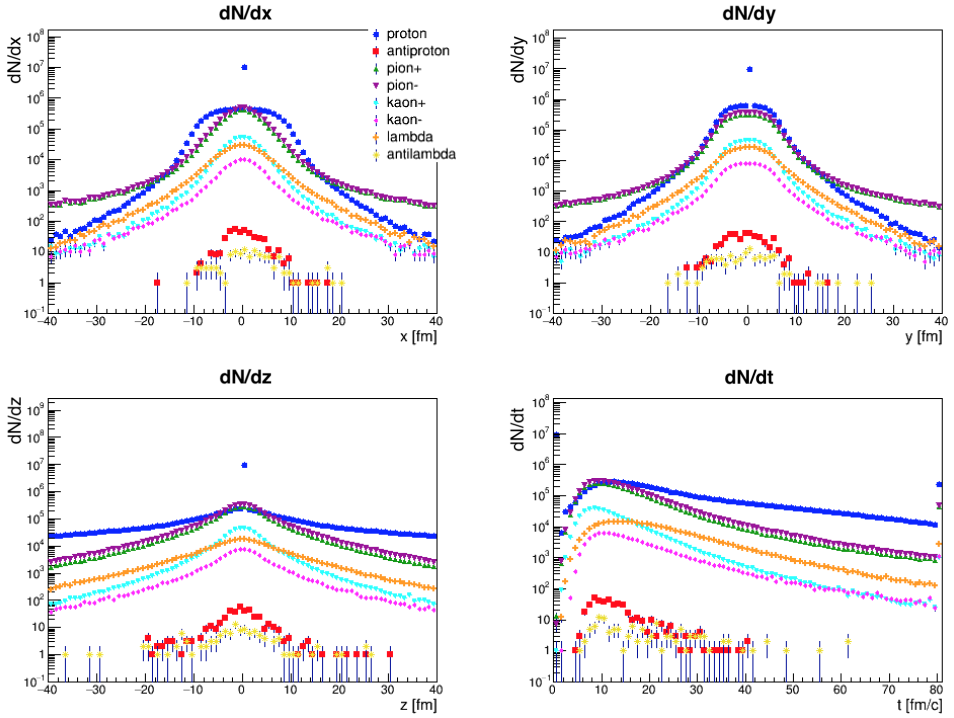

Figure 6.5: Distribution of four-position vector $[x, y, z, t]$ for p, $\overline{p}$, π^+, π^-, κ^+, κ^-, Λ and $\overline{\Lambda}$, for 100 000 Au-Au non-central collisions, for $12[AGeV/c]$ beam momentum.

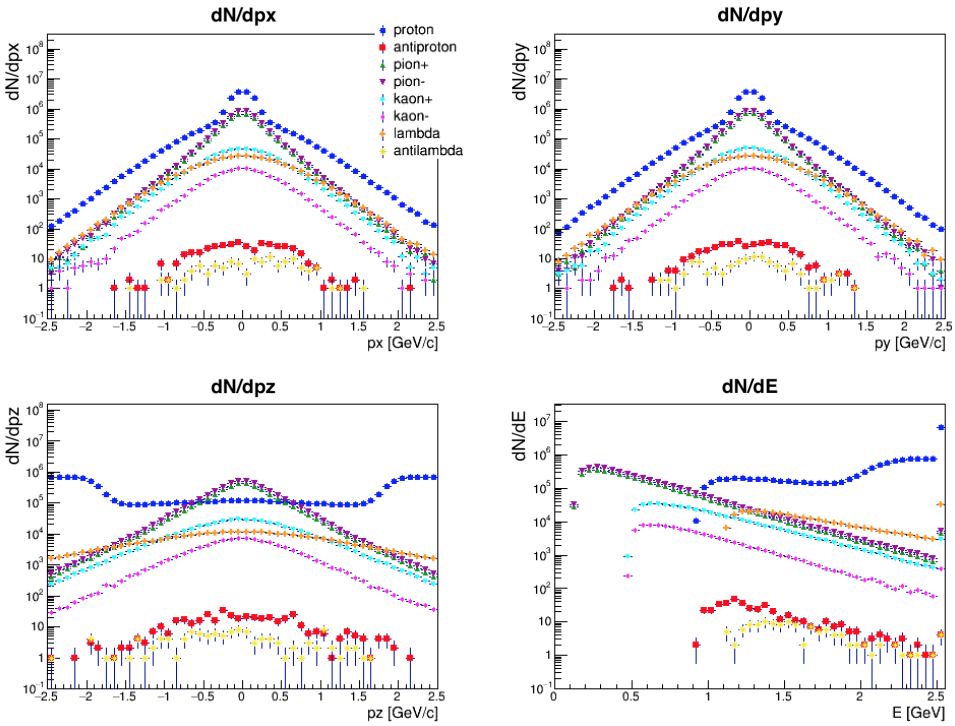

Figure 6.6: Distribution of four-position vector $[p_x, p_y, p_z, E]$ for p, $\overline{p}$, π^+, π^-, κ^+, κ^-, Λ and $\overline{\Lambda}$, for 100 000 Au-Au non-central collisions, for $12[AGeV/c]$ beam momentum.

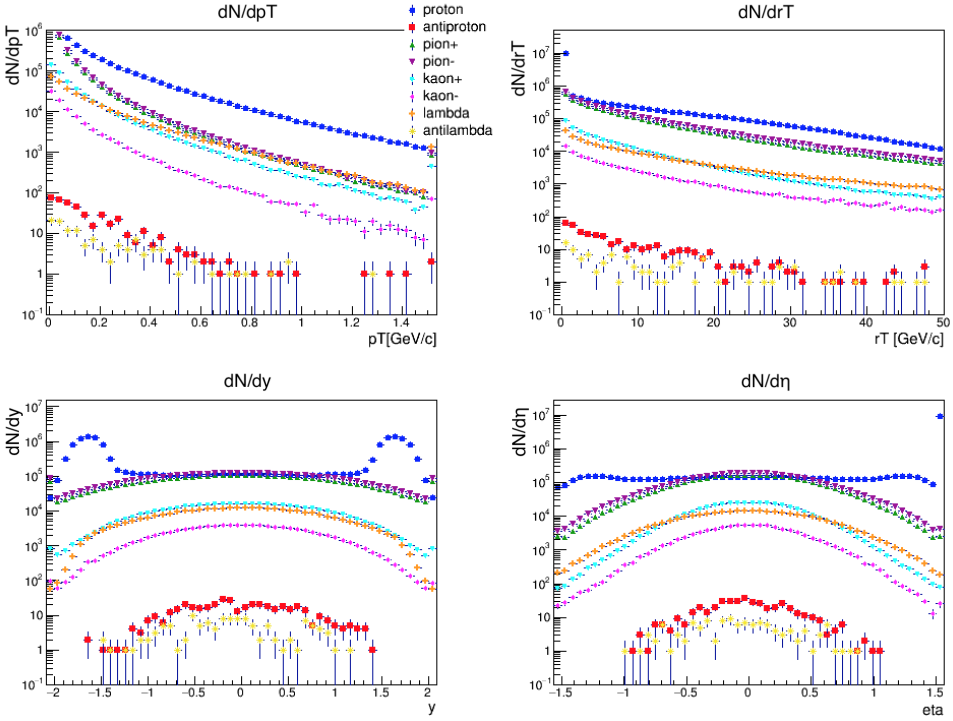

Figure 6.7: Distributions of p_T, r_T, y, η for p, $\overline{p}$, π^+, π^-, κ^+, κ^-, Λ and $\overline{\Lambda}$, for 100 000 Au-Au non-central collisions, for $12[AGeV/c]$ beam momentum.

6.2 Establishing source size for $\pi^-\pi^-$ and $\kappa^+\kappa^+$ correlations

In the Common Production data there is no information about freeze-out. And for that reason, to study the Monte Carlo data generated for the whole CBM collaboration, one must obtain the sizes of the source from the UrQMD data.

As was said before, to study the size of the source one must study the shape of the two-particle correlation function. For that reason $\pi^-\pi^-$ and $\kappa^+\kappa^+$ correlation functions for 48 million central and non-central $Au - Au$ collisions, for $12[AGeV/c]$, $7.95[AGeV/c]$, $4.4[AGeV/c]$, $3.3[AGeV/c]$ beam momentum and four k_T ranges: $(0.15; 0.25)$, $(0.25; 0.35)$, $(0.35; 0.45)$ and $(0.45; 0.60)$ were created. That analysis were also made for the enabled Quantum Statistics interactions only.

The Fig.6.8 shows the scheme of the process of determining the source sizes with each step.

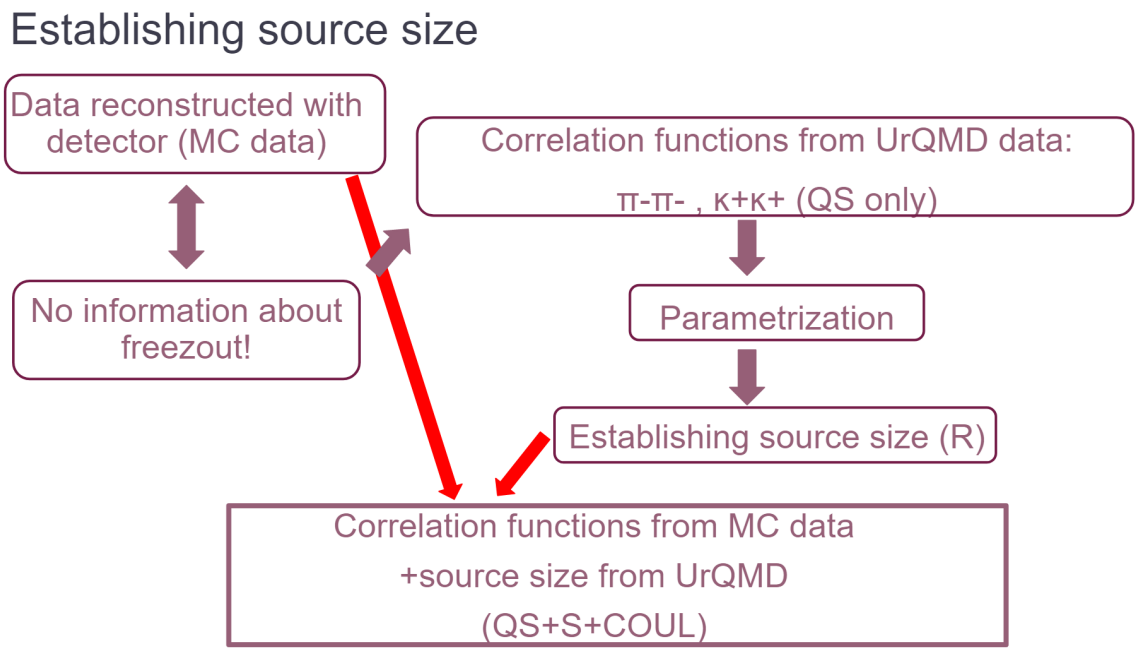

Figure 6.8: The process of establishing the source sizes.

The parametrisation of 1-D $\pi^-\pi^-$ correlation functions for $12[AGeV/c]$ and $3.3[AGeV/c]$ beam momentum, for central and non-central collisions are shown in the Fig.6.9, Fig.6.10, Fig.6.11 and Fig.6.12.

The parametrisation of 1-D $\kappa^+\kappa^+$ correlation functions for $12[AGeV/c]$ and $3.3[AGeV/c]$ beam momentum, for central and non-central collisions are shown in the Fig.6.14, Fig.6.15,

Fig.6.16 and Fig.6.17.

Fig.6.13 and Fig.6.18 show the distribution of measured $\pi^-\pi^-$ and $\kappa^+\kappa^+$ correlation functions source sizes for central (0-10%) and non-central (10-100%) Au-Au collisions for 4 beam momenta: $12[AGeV/c]$, $7.95[AGeV/c]$, $4.4[AGeV/c]$ and $3.3[AGeV/c]$.

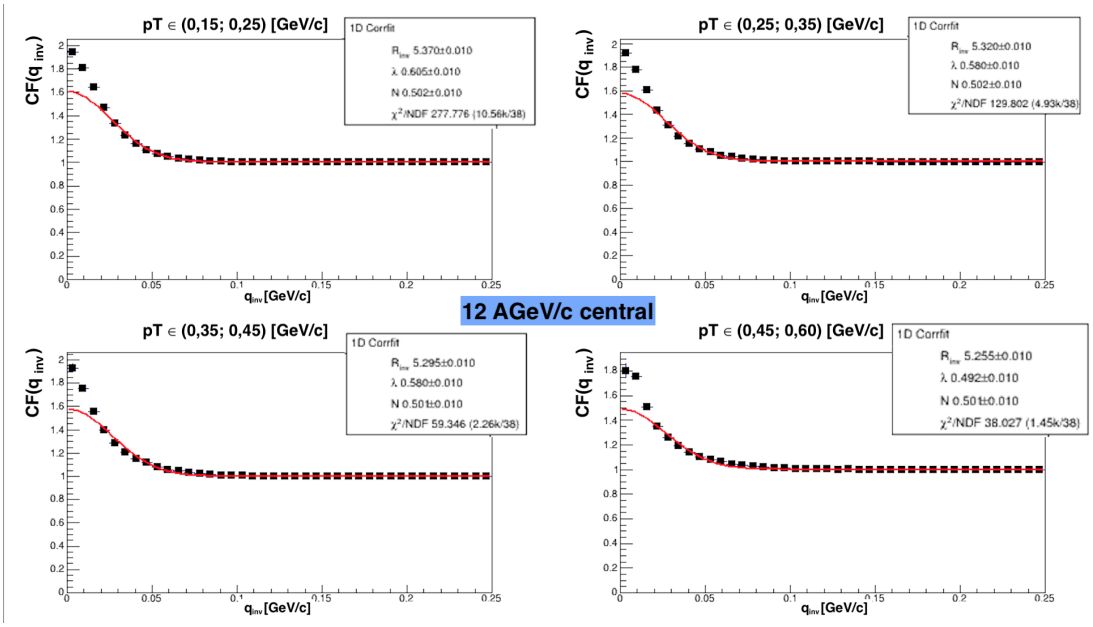

Figure 6.9: Process of determining the source size for $\pi^-\pi^-$ for 12 [AGeV/c], central collisions.

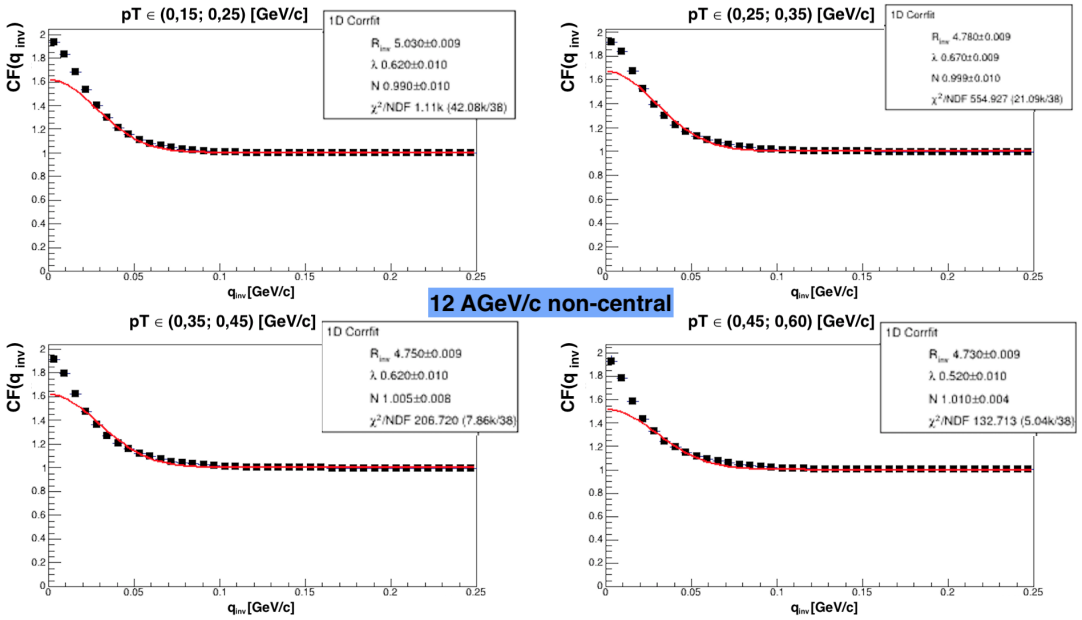

Figure 6.10: Process of determining R size for $\pi^-\pi^-$ for 12 [AGeV/c], non-central collisions

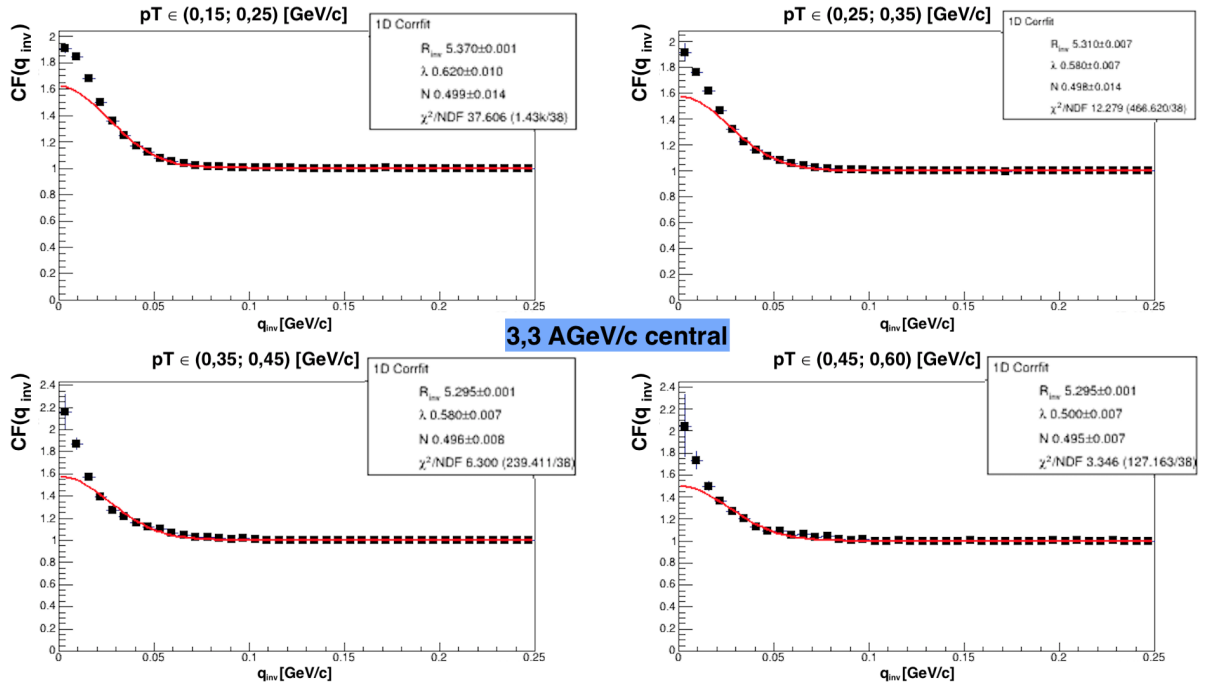

Figure 6.11: Process of determining R size for $\pi^-\pi^-$ for 3.3 [AGeV/c], central collisions

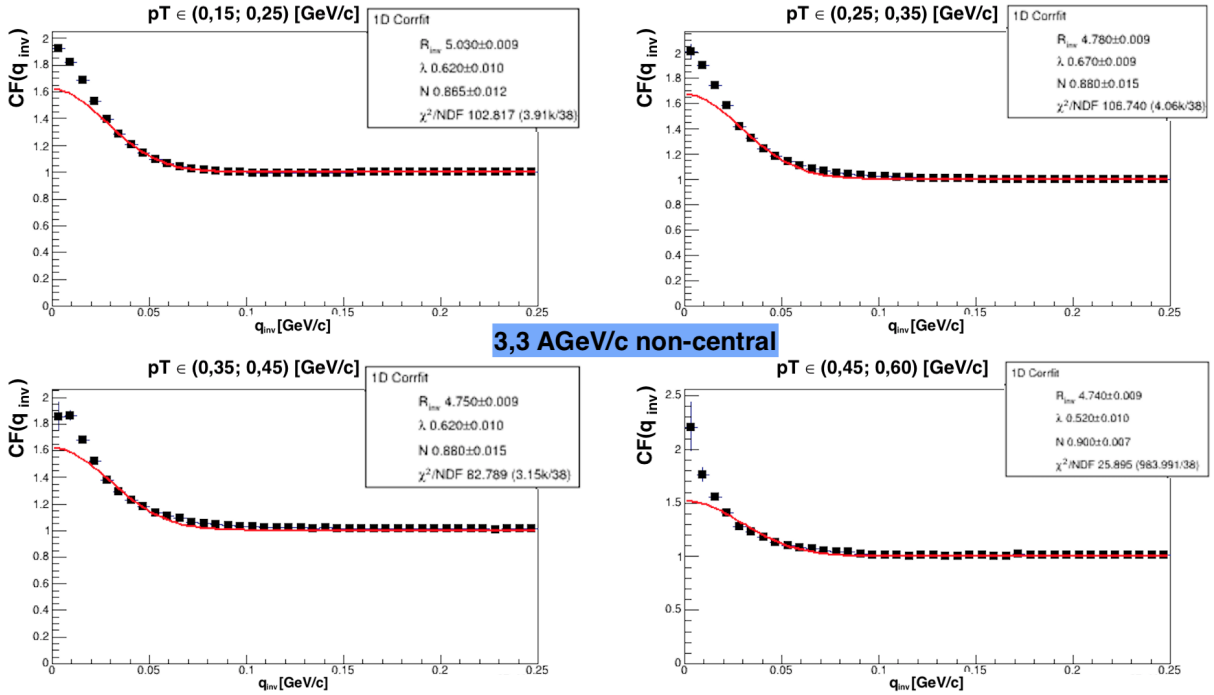

Figure 6.12: Process of determining R size for $\pi^-\pi^-$ for 3.3 [AGeV/c], non-central collisions

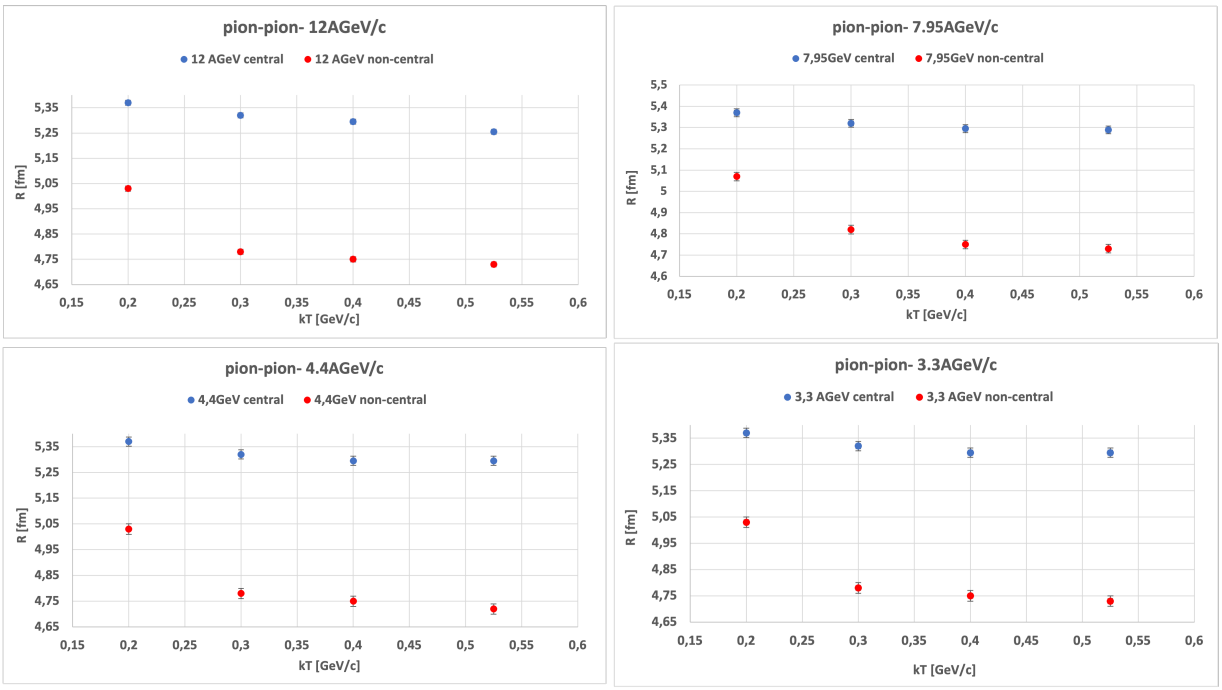

Figure 6.13: Distributions of measured $\pi^-\pi^-$ correlation functions source sizes for central (0-10%) and non-central (10-100%) Au-Au collisions for 4 beam momenta: $12[AGeV/c]$, $7.95[AGeV/c]$, $4.4[AGeV/c]$ and $3.3[AGeV/c]$.

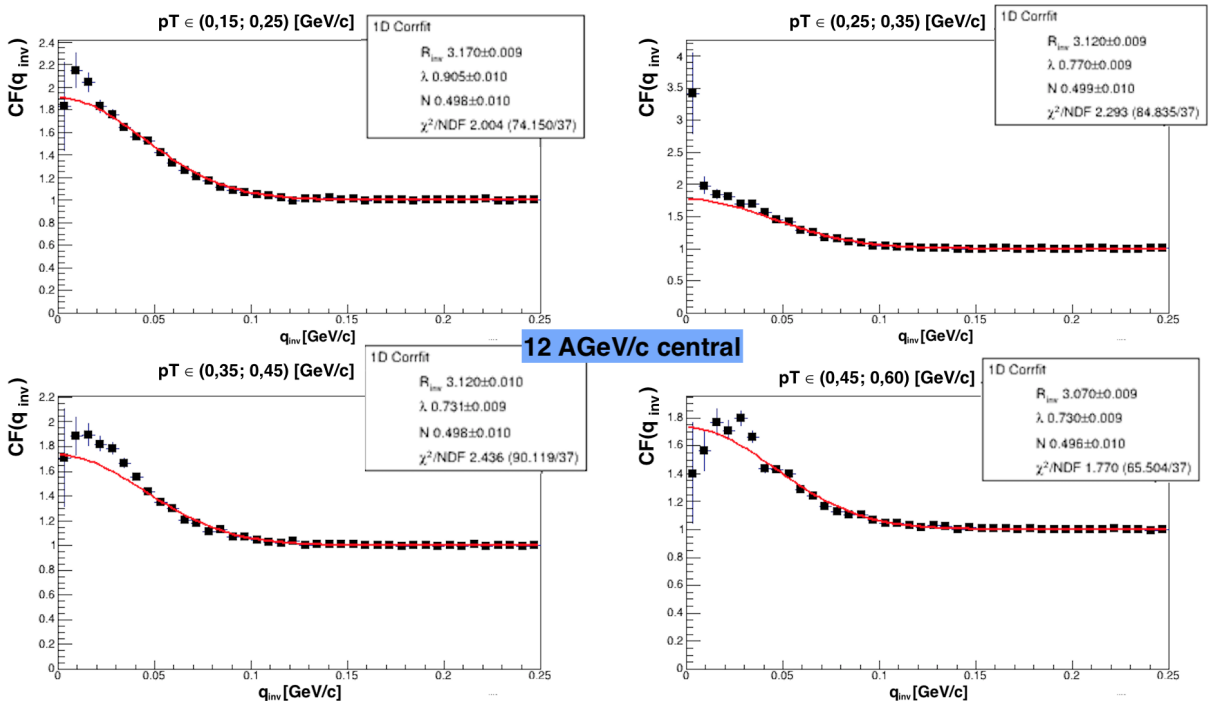

Figure 6.14: Process of determining R size for $\kappa^+\kappa^+$ for 12 [AGeV/c], central collisions.

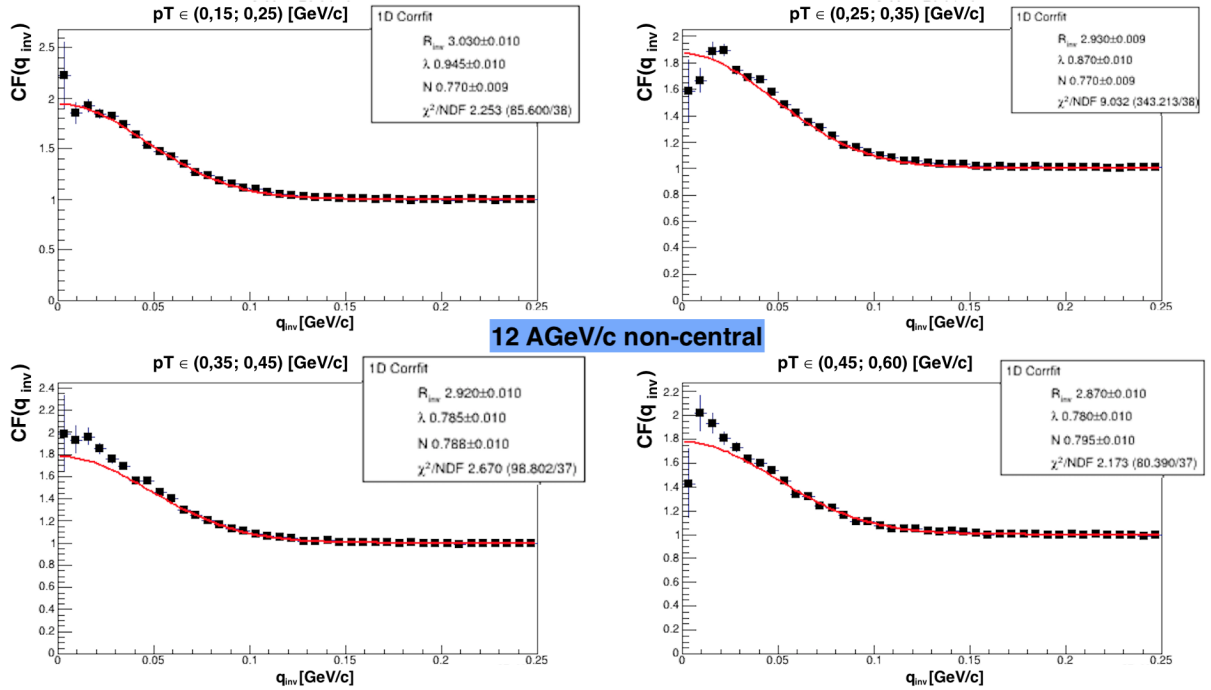

Figure 6.15: Process of determining R size for $\kappa^+\kappa^+$ for 12 [AGeV/c], non-central collisions.

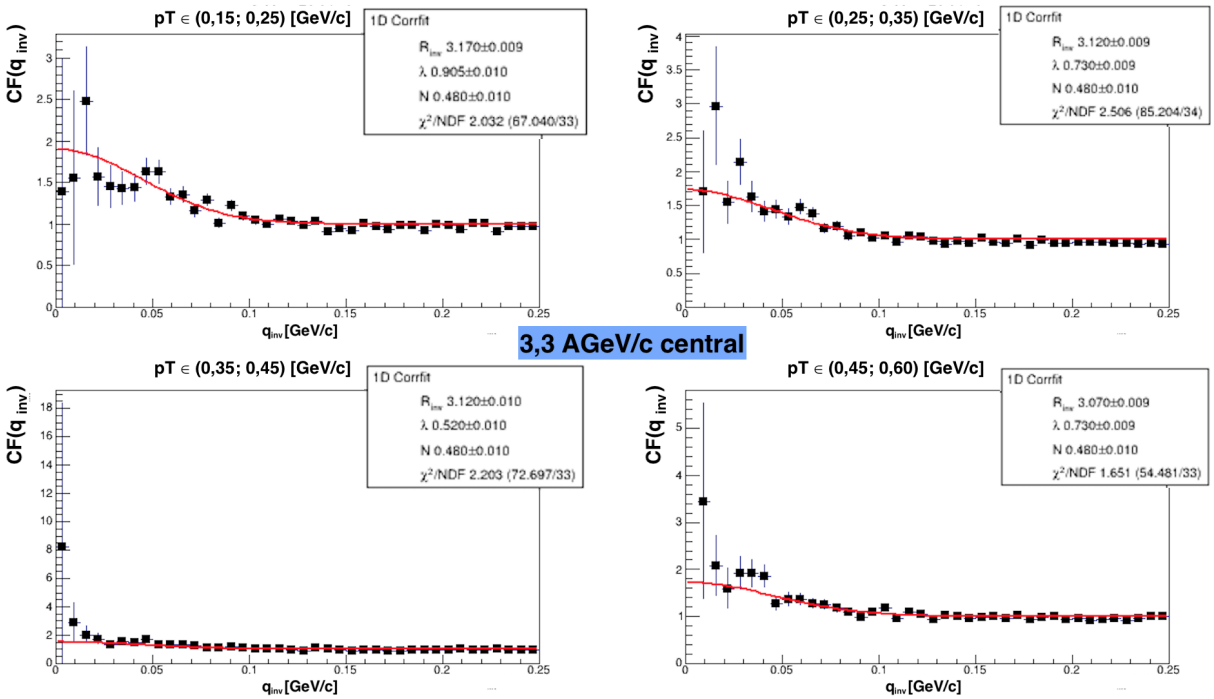

Figure 6.16: Process of determining R size for $\kappa^+\kappa^+$ for 3.3 [AGeV/c], central collisions.

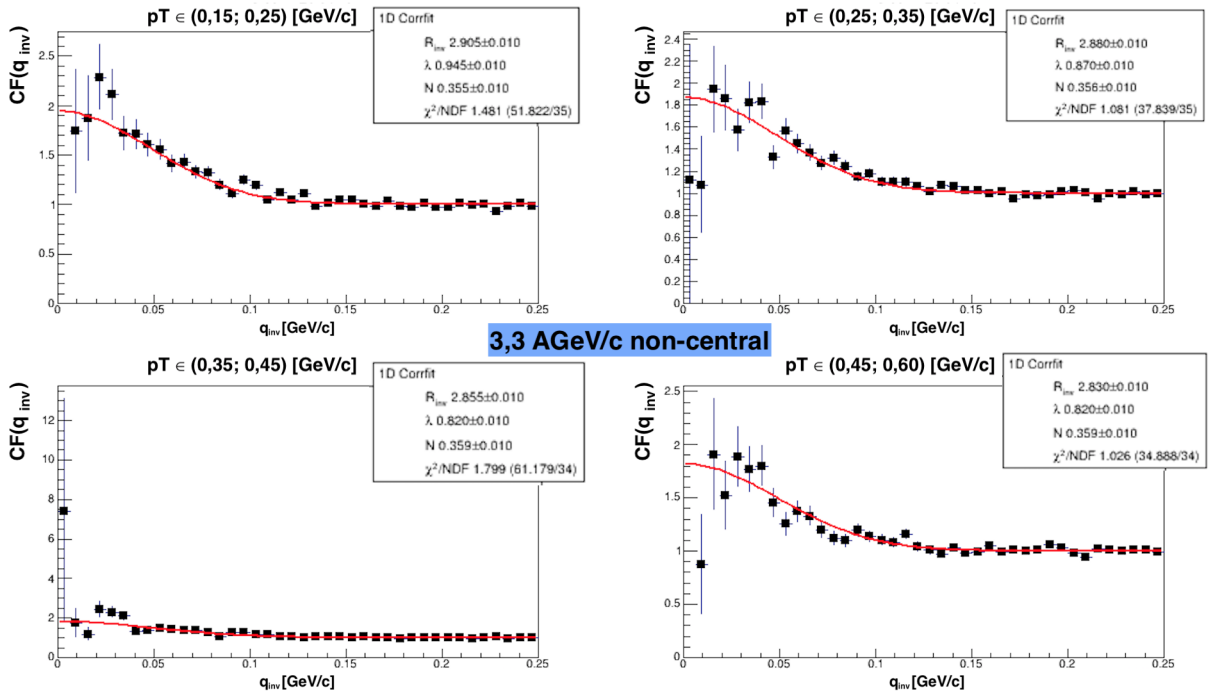

Figure 6.17: Process of determining R size for $\kappa^+\kappa^+$ for 3.3 [AGeV/c], non-central collisions

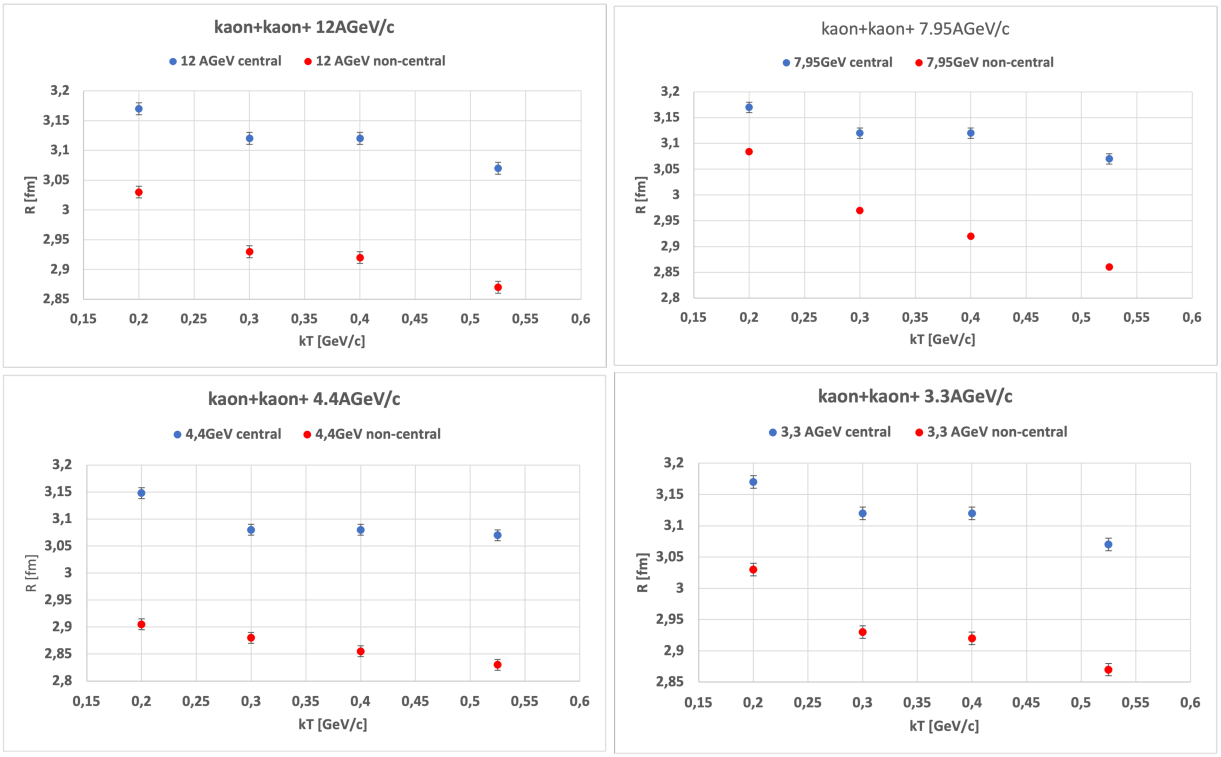

Figure 6.18: Distributions of measured $\kappa^+\kappa^+$ correlation functions source sizes for central (0-10%) and non-central (10-100%) Au-Au collisions for 4 beam momenta: $12[AGeV/c]$, $7.95[AGeV/c]$, $4.4[AGeV/c]$ and $3.3[AGeV/c]$.

Table 6.3: Established R sizes and λ values for $\pi^-\pi^-$ for 12 [AGeV/c] Au-Au collisions, 4 k_T ranges and 2 centralities. Source sizes are given in [fm].

k_T ∈		12 [AGeV/c] central	12 [AGeV/c] non-central
(0.15 ; 0.25)	R	5.370	5.030
	λ	0.605	0.620
(0.25 ; 0.35)	R	5.320	4.780
	λ	0.580	0.670
(0.35 ; 0.45)	R	5.295	4.750
	λ	0.580	0.620
(0.45 ; 0.65)	R	5.255	4.730
	λ	0.492	0.520

Table 6.4: Established R sizes and λ values for $\pi^-\pi^-$ for 7.95 [AGeV/c] Au-Au collisions, 4 k_T ranges and 2 centralities. Source sizes are given in [fm].

k_T ∈		7.95 [AGeV/c] central	7.95 [AGeV/c] non-central
(0.15 ; 0.25)	R	5.370	5.070
	λ	0.610	0.611
(0.25 ; 0.35)	R	5.320	4.820
	λ	0.580	0.638
(0.35 ; 0.45)	R	5.295	4.730
	λ	0.580	0.604
(0.45 ; 0.65)	R	5.289	4.730
	λ	0.497	0.520

Table 6.5: Established R sizes and λ values for $\pi^-\pi^-$ for 4.4 [AGeV/c] Au-Au collisions, 4 k_T ranges and 2 centralities. Source sizes are given in [fm].

k_T ∈		4.4 [AGeV/c] central	4.4 [AGeV/c] non-central
(0.15 ; 0.25)	R	5.370	5.030
	λ	0.617	0.620
(0.25 ; 0.35)	R	5.320	4.780
	λ	0.580	0.670
(0.35 ; 0.45)	R	5.295	4.750
	λ	0.580	0.620
(0.45 ; 0.65)	R	5.295	4.720
	λ	0.488	0.480

Table 6.6: Established R sizes and λ values for $\pi^-\pi^-$ for 3.3 [AGeV/c] Au-Au collisions, 4 k_T ranges and 2 centralities. Source sizes are given in [fm].

k_T ∈		3.3 [AGeV/c] central	3.3 [AGeV/c] non-central
(0.15 ; 0.25)	R	5.370	5.030
	λ	0.619	0.620
(0.25 ; 0.35)	R	5.320	4.780
	λ	0.580	0.670
(0.35 ; 0.45)	R	5.295	4.750
	λ	0.580	0.604
(0.45 ; 0.65)	R	5.295	4.730
	λ	0.494	0.520

Table 6.7: Established R sizes and λ values for $\kappa^+\kappa+^-$ for 12 [AGeV/c] Au-Au collisions, 4 k_T ranges and 2 centralities. Source sizes are given in [fm].

k_T ∈		12 [AGeV/c] central	12 [AGeV/c] non-central
(0.15 ; 0.25)	R	3.170	3.030
	λ	0.905	0.945
(0.25 ; 0.35)	R	3.120	2.930
	λ	0.770	0.870
(0.35 ; 0.45)	R	3.120	2.920
	λ	0.730	0.785
(0.45 ; 0.65)	R	3.070	2.870
	λ	0.730	0.780

Table 6.8: Established R sizes and λ values for $\kappa^+\kappa+^-$ for 7.95 [AGeV/c] Au-Au collisions, 4 k_T ranges and 2 centralities. Source sizes are given in [fm].

k_T ∈		7.95 [AGeV/c] central	7.95 [AGeV/c] non-central
(0.15 ; 0.25)	R	3.170	3.084
	λ	0.905	0.928
(0.25 ; 0.35)	R	3.120	2.970
	λ	0.770	0.836
(0.35 ; 0.45)	R	3.120	2.920
	λ	0.765	0.820
(0.45 ; 0.65)	R	3.070	2.860
	λ	0.730	0.780

Table 6.9: Established R sizes and λ values for $\kappa^{+}\kappa{+}^{-}$ for 4.4 [AGeV/c] Au-Au collisions, 4 k_T ranges and 2 centralities. Source sizes are given in [fm].

k_T ϵ		4.4 [AGeV/c] central	4.4 [AGeV/c] non-central
(0.15 ; 0.25)	R	3.148	2.905
	λ	0.945	0.945
(0.25 ; 0.35)	R	3.080	2.880
	λ	0.770	0.870
(0.35 ; 0.45)	R	3.080	2.855
	λ	0.770	0.820
(0.45 ; 0.65)	R	3.070	2.830
	λ	0.770	0.820

Table 6.10: Established R sizes and λ values for $\kappa^{+}\kappa{+}^{-}$ for 3.3 [AGeV/c] Au-Au collisions, 4 k_T ranges and 2 centralities. Source sizes are given in [fm].

k_T ϵ		3.3 [AGeV/c] central	3.3 [AGeV/c] non-central
(0.15 ; 0.25)	R	3.170	2.905
	λ	0.905	0.945
(0.25 ; 0.35)	R	3.120	2.880
	λ	0.730	0.870
(0.35 ; 0.45)	R	3.120	2.855
	λ	0.520	0.820
(0.45 ; 0.65)	R	3.070	2.830
	λ	0.730	0.820

Tab.6.11 and Tab.6.12 shows the values of the $\pi^-\pi^-$ and $\kappa^+\kappa^+$ correlations source sizes obtained by different parametrization of the functions.

UrQMD form Virgo means that data was generated on CBM cluster called *Virgo*, while *UrQMD from DWARF* is data generated on Warsaw University of Techlogy cluster called *DWARF*. Both data was simulated with the same parameters. *BWIntegrate* is a software using Richard Lednicky's weights.

Table 6.11: Comparison between results of obtained R sizes for UrQMD data from Virgo cluster and DWARF cluster and different fitting formulas: NicaFemto and BWIntegrate fitting methods for $\pi^-\pi^-$, 12 [AGeV] beam momentum.

data	fit	R [fm] s for central collisions	R [fm] for non-central collisions
UrQMD form Virgo	NicaFemto	5.37	5.03
UrQMD from Virgo	BWIntegrate	5.53	4.84
UrQMD from DWARF	BWIntegrate	4.90	3.70

Table 6.12: Comparison between results of obtained R sizes for UrQMD data from Virgo cluster and DWARF cluster and different fitting formulas: NicaFemto and BWIntegrate fitting methods for $\kappa^+\kappa^+$, 12 [AGeV] beam momentum

data	fit	R [fm] for central collisions	R [fm] for non-central collisions
UrQMD form Virgo	NicaFemto	3.17	3.03
UrQMD from Virgo	BWIntegrate	3.37	2.90
UrQMD from DWARF	BWIntegrate	3.59	2.84

After obtaining the radius size of the source from the UrQMD data, one can use this information to create the correlation functions from Common Production Monte Carlo data with added radius size.

Fig.6.19 shows an example of the $\pi^-\pi^-$ correlation function from Common Production data, for 5 million central $Au - Au$ collisions for $12[AGeV/c]$ beam momentum with the source radius size established in UrQMD data analysis.

Fig.6.20 shows an example of the $\kappa^+\kappa+$ correlation function from Common Production data, for 10 million central $Au - Au$ collisions for $12[AGeV/c]$ beam momentum with the source radius size established in UrQMD data analysis.

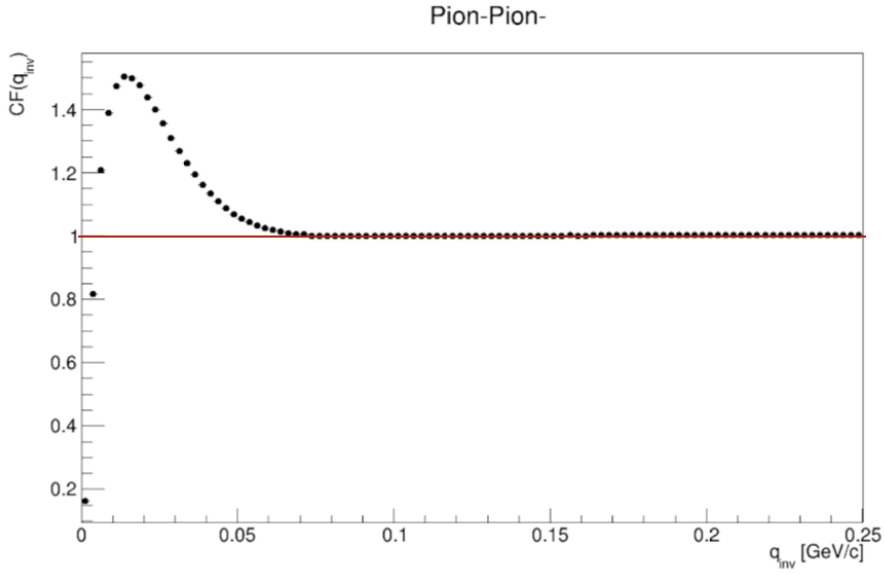

Figure 6.19: The $\pi^{-}\pi^{-}$ correlation function for 12 [AGeV/c] beam momentum, 5 million central $Au - Au$ collisions, from Common production data with R established in previous analysis.

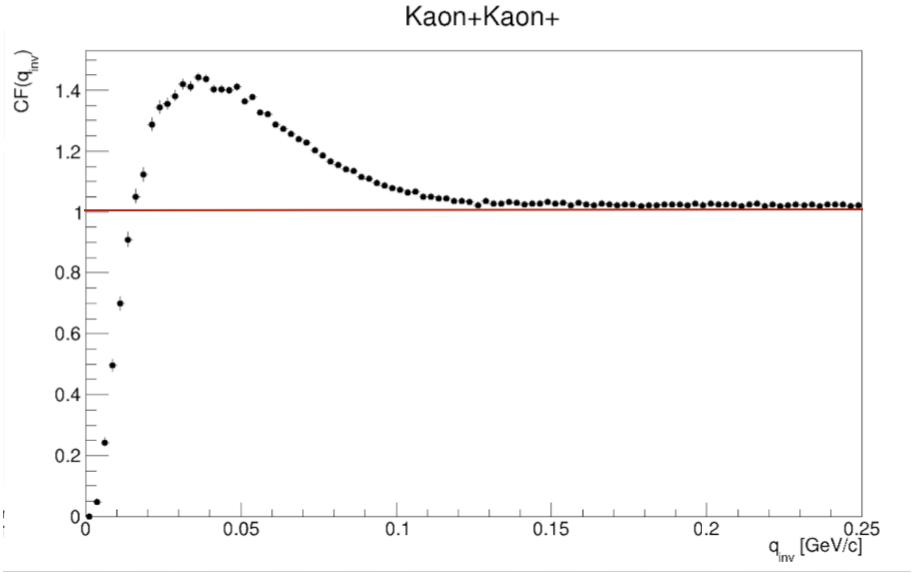

Figure 6.20: The $\kappa^{+}\kappa^{+}$ correlation function for 12 [AGeV/c] beam momentum, 10 million central $Au - Au$ collisions, from Common production data with R established in previous analysis.

6.3 Establishing statistics

This part of the thesis focuses on estimation of the required number of $Au-Au$ collisions needed to obtain correlation functions with systematic error of 10%, 5% and 1% for the p, κ and π particle pairs, for two ranges of centrality and four values of beam momentum: $12[AGeV/c]$, $7.95[AGeV/c]$, $4.4[AGeV/c]$ and $3.3[AGeV/c]$, for UrQMD data.

The aim of this part of the study was to gain information about nonidentical particles pairs correlation functions in Monte Carlo simulations for the CBM experiment at FAIR, which is currently under construction and it will be launched in 2025. Until then one can prepare for the launch by carrying a number of tasks related to Monte Carlo simulations of heavy ion collisions process, such as estimation of the amount of data needed to perform basic femtoscopic analyzes.

6.3.1 Establishing needed statistics by analysis of first 10 bins of correlation function

This method to estimate the necessary statistics to obtain systematic error of given value is based on analysing correlation function in the area of $k*$ where the correlation effect occurs.

The process of this type of analysis starts with creating a correlation function from UrQMD data and establishing the k^* area of the correlation effects.

On the right side of Fig.6.21 there is an example of $\pi^+\kappa^+$ correlation function with marked area of correlation effects. Next, one creates correlation functions in established $k*$ range, 10 bins each, for just one event. On the left side of the Fig.6.21 there is an example of π^+p correlation function in the established $k*$ range with 10 bins. Then, one can read the number of pairs from numerator of the function. By repeating this one can obtain the distribution of the number of pairs per one event. By calculating the mean number and the standard deviation σ of pairs per one event per one bin one can calculate the required number of events by transforming the formula:

$$\begin{aligned} \frac{1}{\sqrt{N}} &= 10\% \\ N &= 100 \\ N_{cor} &= 100 \cdot 10 = 1000 \end{aligned} \tag{6.1}$$

The formula 6.1 is an example of calculation to obtain a number of events for an systematic error of 10%, where N is the number of needed events in 1 bin and N_{cor} is the number of needed events per 10 bins, which is the number of bins used in this analysis.

To calculate required number of events for obtaining the systematic error at given value

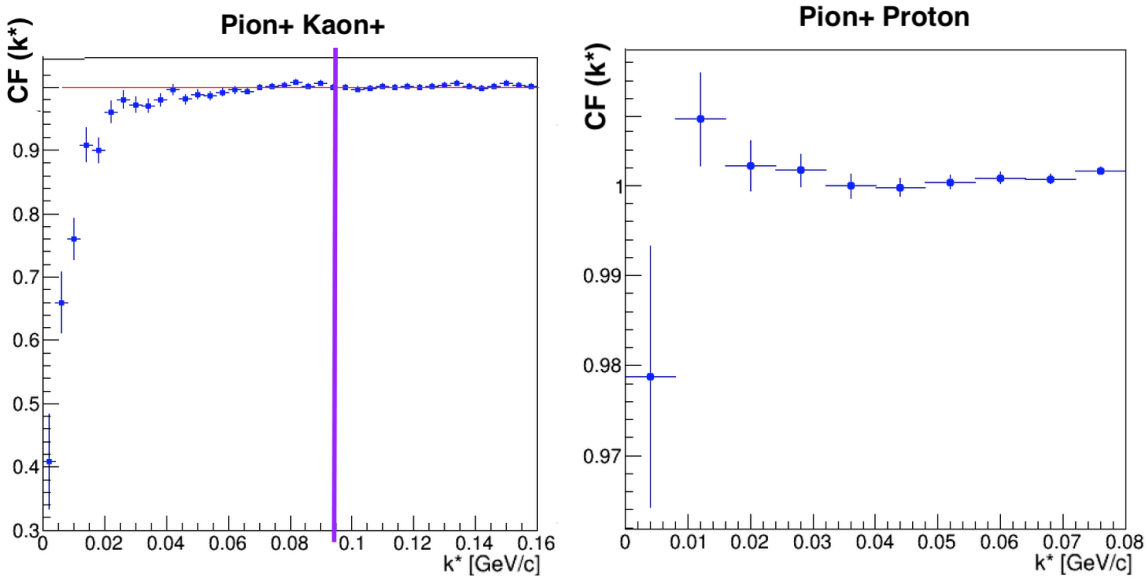

Figure 6.21: The $\pi^+\kappa^+$ correlation function with marked $k*$ area of correlation effects (right). The π^+p correlation function in the $k*$ region of correlation effects, made with 10 bins to examine needed statistics (left).

one can finally use the formula 6.2, where $\overline{N}$ is the mean number of pairs per one event and N_{ev} is the required number of events for obtaining the correlation function with systematic error of given value (10%, 5% or 1% in following calculations).

$$\frac{N_{cor}}{\overline{N}} = N_{ev} \tag{6.2}$$

The distributions of the mean value of pairs per one event for $p\kappa^+$, $\pi^+\kappa^+$ and π^+p particle pairs, for central and non-central Au-Au collisions, for $12[AGeV/c]$, $7.95[AGeV/c]$, $4.4[AGeV/c]$ and $3.3[AGeV/c]$ beam momentum were shown in the figures: Fig.6.22, Fig.6.23, Fig.6.24, Fig.6.25, Fig.6.26, Fig.6.27.

Additionally, the mean value and the standard deviation of the number of pairs in the first 10 bins of the studied correlation functions were presented in the tables: Tab.6.13, Tab.6.15, Tab.6.17, Tab.6.19, Tab.6.21, Tab.6.23.

Finally, the estimated number of events needed to obtain the systematic error of order of 10%, 5% or 1% for $p\kappa^+$, $\pi^+\kappa^+$ and π^+p correlation functions, for central and non-central $Au-Au$ collisions for $12[AGeV/c]$, $7.95[AGeV/c]$, $4.4[AGeV/c]$ and $3.3[AGeV/c]$ beam momentum were presented in the tables: Tab.6.14, Tab.6.16, Tab.6.18, Tab.6.20, Tab.6.22, Tab.6.24.

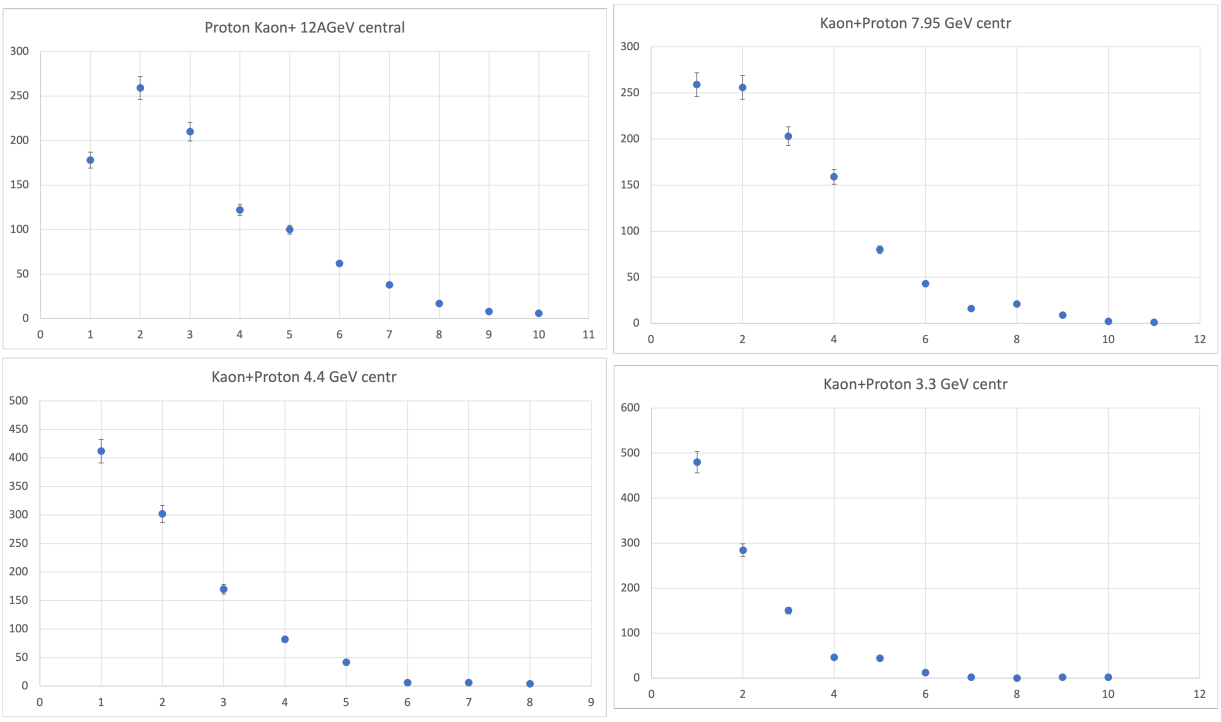

Figure 6.22: A distributions of number of κ^+p particle pairs in the first 10 bins for 12 [AGeV/c], 7.95 [AGeV/c], 4.4 [AGeV/c] and 3.3 [AGeV/c], central collisions.

Table 6.13: Mean number of κ^+p particle pairs in the first 10 bins with standard deviation σ for 12 [AGeV/c], 7.95 [AGeV/c], 4.4 [AGeV/c] and 3.3 [AGeV/c], central collisions.

κ^+p central				
	12 [AGeV/c]	7,95 [AGeV/c]	4,4 [AGeV/c]	3,3 [AGeV/c]
mean	2,697	2,432	1,811	1,681
σ	1,902	1,820	1,274	1,281

Table 6.14: The established number of events needed to obtain the statistical error bar of 10%, 5% and 1% for κ^+p correlation function for 12 [AGeV/c], 7.95 [AGeV/c], 4.4 [AGeV/c] and 3.3 [AGeV/c], central collisions.

κ^+p central				
	12 [AGeV/c]	7,95 [AGeV/c]	4,4 [AGeV/c]	3,3 [AGeV/c]
10%	371	412	553	595
5%	1 484	1 645	2 209	2 380
1%	37 081	41 119	55 220	59 500

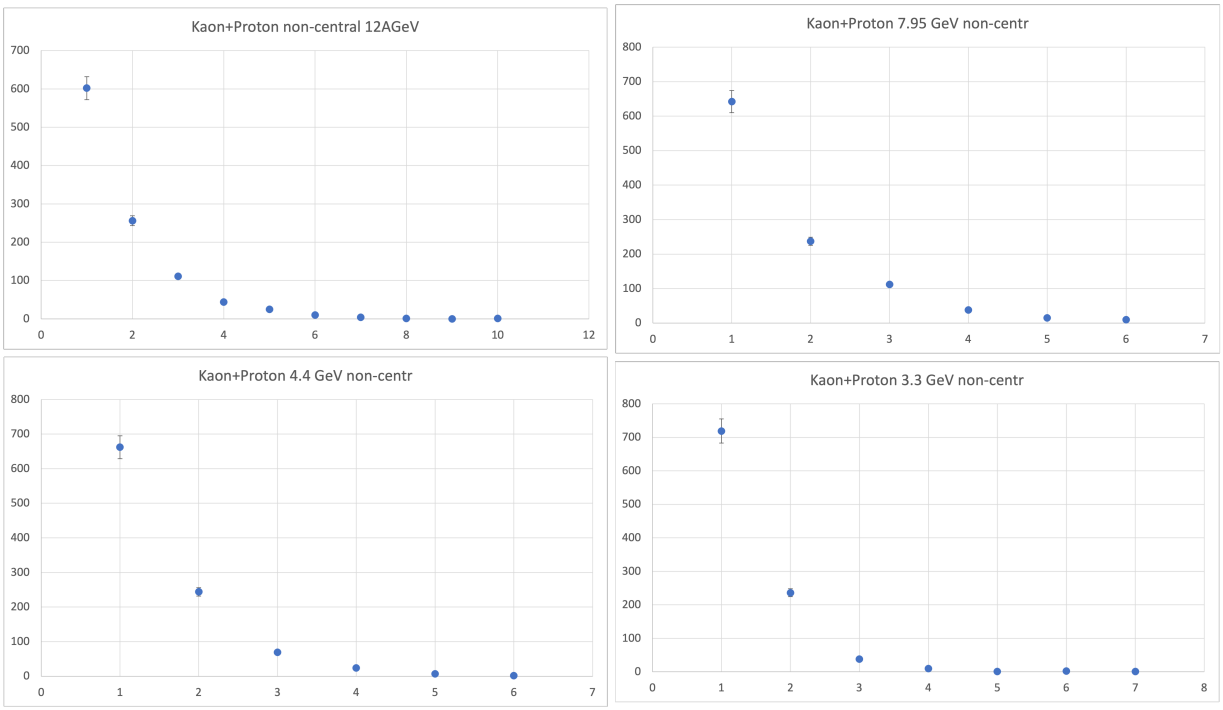

Figure 6.23: A distribution of number of κ^+p particle pairs in the first 10 bins for 12 [AGeV/c], 7.95 [AGeV/c], 4.4 [AGeV/c] and 3.3 [AGeV/c], non-central collisions.

Table 6.15: Mean number of κ^+p particle pairs in the first 10 bins with standard deviation σ for 12 [AGeV/c], 7.95 [AGeV/c], 4.4 [AGeV/c] and 3.3 [AGeV/c], non-central collisions.

κ^+p non-central				
	12 [AGeV/c]	7,95 [AGeV/c]	4,4 [AGeV/c]	3,3 [AGeV/c]
mean	1,505	1,442	1,337	1,252
σ	1,158	1,058	0,808	0,668

Table 6.16: The established number of events needed to obtain the statistical error bar of 10%, 5% and 1% for κ^+p correlation function for 12 [AGeV/c], 7.95 [AGeV/c], 4.4 [AGeV/c] and 3.3 [AGeV/c], non-central collisions.

κ^+p non-central				
	12 [AGeV/c]	7,95 [AGeV/c]	4,4 [AGeV/c]	3,3 [AGeV/c]
10%	665	694	748	799
5%	2 659	2 775	2 991	3 195
1%	66 456	69 354	74 772	79 871

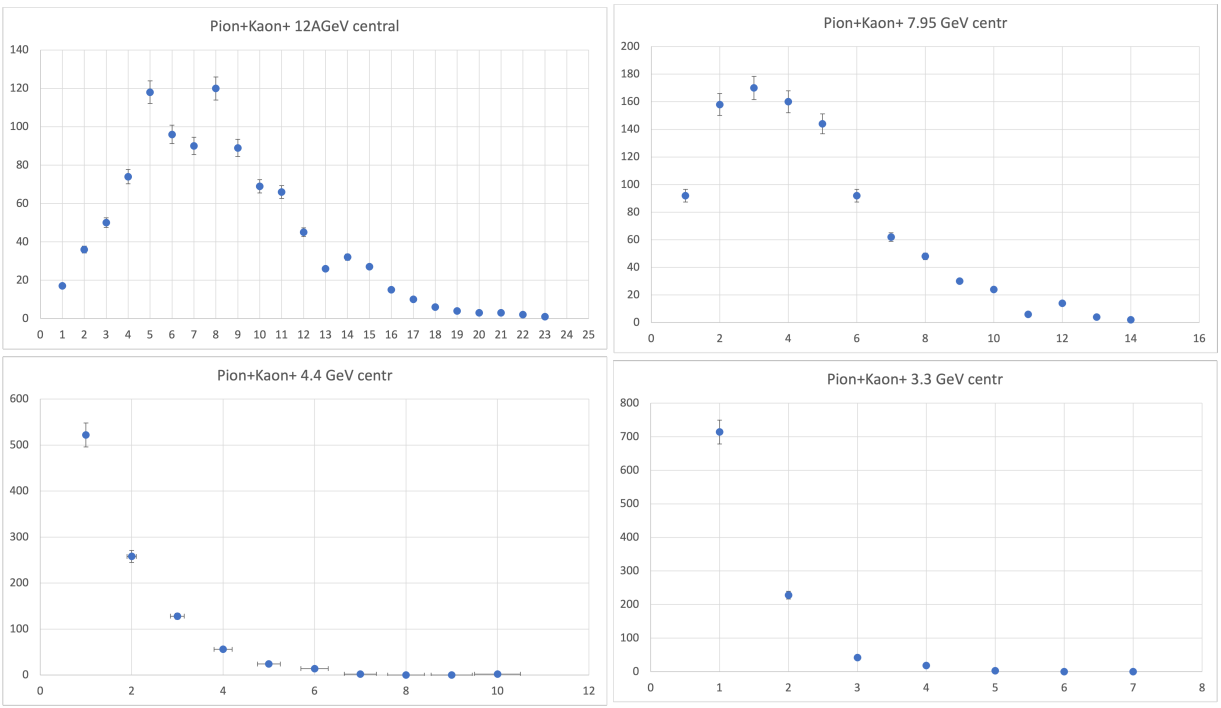

Figure 6.24: A distribution of number of $\pi^+\kappa^+$ particle pairs in the first 10 bins for 12 [AGeV/c], 7.95 [AGeV/c], 4.4 [AGeV/c] and 3.3 [AGeV/c], central collisions.

Table 6.17: Mean number of $\pi^+\kappa^+$ particle pairs in the first 10 bins with standard deviation σ for 12 [AGeV/c], 7.95 [AGeV/c], 4.4 [AGeV/c] and 3.3 [AGeV/c], central collisions.

$\pi^+\kappa^+$ central				
	12 [AGeV/c]	7,95 [AGeV/c]	4,4 [AGeV/c]	3,3 [AGeV/c]
mean	7,013	3,718	1,594	1,262
σ	3,978	2,561	1,211	0,679

Table 6.18: The established number of events needed to obtain the statistical error bar of 10%, 5% and 1% for $\pi^+\kappa^+$ correlation function for 12 [AGeV/c], 7.95 [AGeV/c], 4.4 [AGeV/c] and 3.3 [AGeV/c], central collisions.

$\pi^+\kappa^+$ central				
	12 [AGeV/c]	7,95 [AGeV/c]	4,4 [AGeV/c]	3,3 [AGeV/c]
10%	143	269	628	793
5%	571	1 076	2 509	3 170
1%	14 260	26 897	62 720	79 232

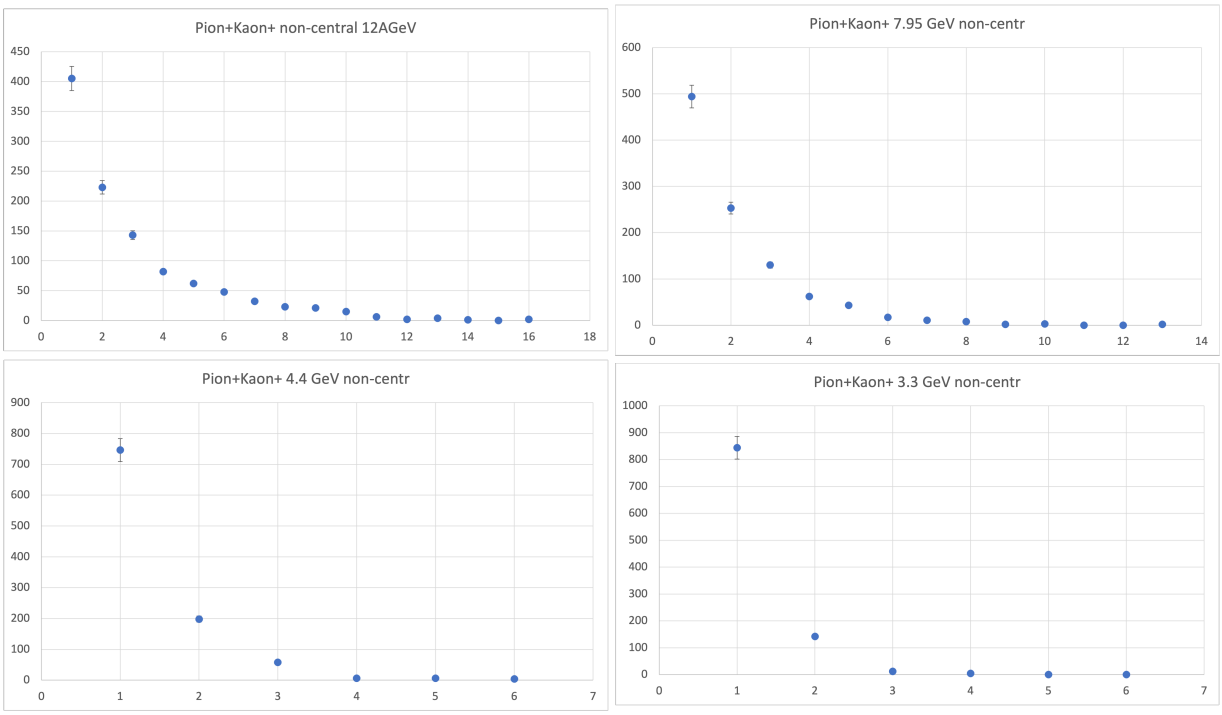

Figure 6.25: A distribution of number of $\pi^+\kappa^+$ particle pairs in the first 10 bins for 12 [AGeV/c], 7.95 [AGeV/c], 4.4 [AGeV/c] and 3.3 [AGeV/c], non-central collisions.

Table 6.19: Mean number of $\pi^+\kappa^+$ particle pairs in the first 10 bins with standard deviation σ for 12 [AGeV/c], 7.95 [AGeV/c], 4.4 [AGeV/c] and 3.3 [AGeV/c], non-central collisions.

$\pi^+\kappa^+$ non-central				
	12 [AGeV/c]	7,95 [AGeV/c]	4,4 [AGeV/c]	3,3 [AGeV/c]
mean	2,194	1,724	1,249	1,124
σ	2,482	1,596	0,729	0,440

Table 6.20: The established number of events needed to obtain the statistical error bar of 10%, 5% and 1% for $\pi^+\kappa^+$ correlation function for 12 [AGeV/c], 7.95 [AGeV/c], 4.4 [AGeV/c] and 3.3 [AGeV/c], non-central collisions.

$\pi^+\kappa^+$ non-central				
	12 [AGeV/c]	7,95 [AGeV/c]	4,4 [AGeV/c]	3,3 [AGeV/c]
10%	456	580	801	890
5%	1 824	2 321	3 204	3 559
1%	45 589	58 004	80 083	88 966

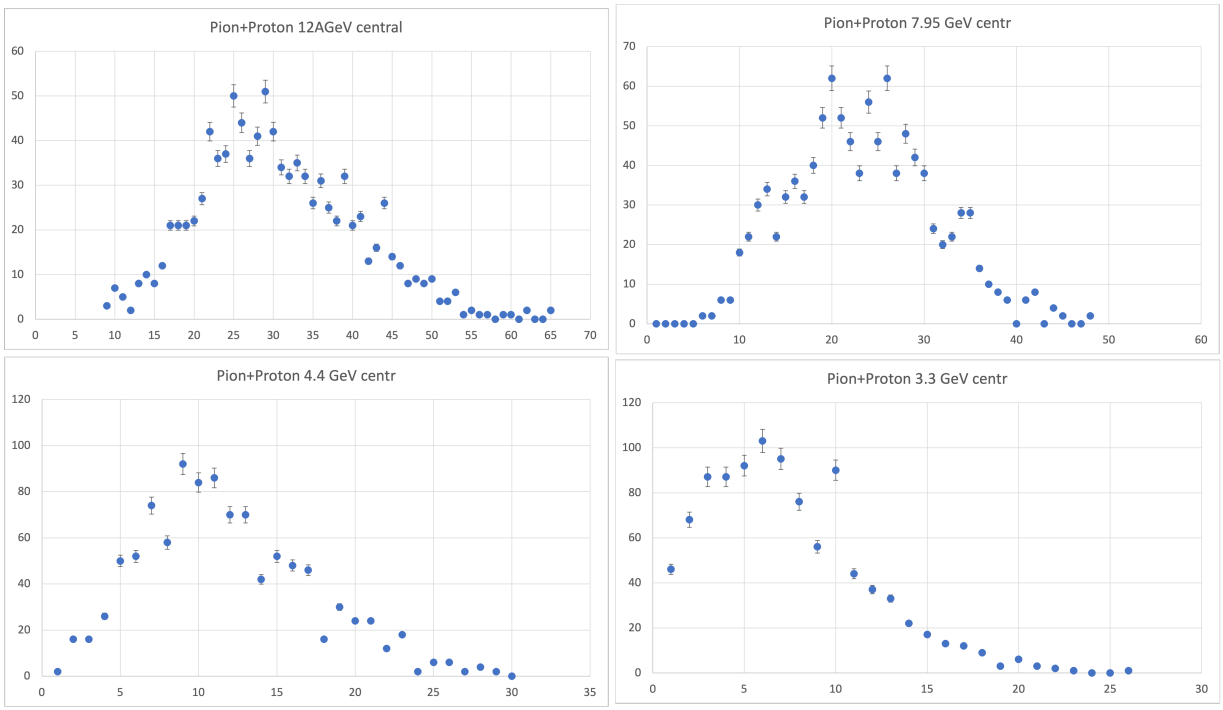

Figure 6.26: A distribution of number of π^+p particle pairs in the first 10 bins for 12 [AGeV/c], 7.95 [AGeV/c], 4.4 [AGeV/c] and 3.3 [AGeV/c], central collisions.

Table 6.21: Mean number of π^+p particle pairs in the first 10 bins with standard deviation σ for 12 [AGeV/c], 7.95 [AGeV/c], 4.4 [AGeV/c] and 3.3 [AGeV/c], central collisions.

π^+p central				
	12 [AGeV/c]	7,95 [AGeV/c]	4,4 [AGeV/c]	3,3 [AGeV/c]
mean	28,955	22,047	10,463	5,996
σ	9,775	7,664	5,320	4,289

Table 6.22: The established number of events needed to obtain the statistical error bar of 10%, 5% and 1% for π^+p correlation function for 12 [AGeV/c], 7.95 [AGeV/c], 4.4 [AGeV/c] and 3.3 [AGeV/c], central collisions.

π^+p central				
	12 [AGeV/c]	7,95 [AGeV/c]	4,4 [AGeV/c]	3,3 [AGeV/c]
10%	35	46	96	167
5%	139	182	383	668
1%	3 454	4 536	9 558	16 678

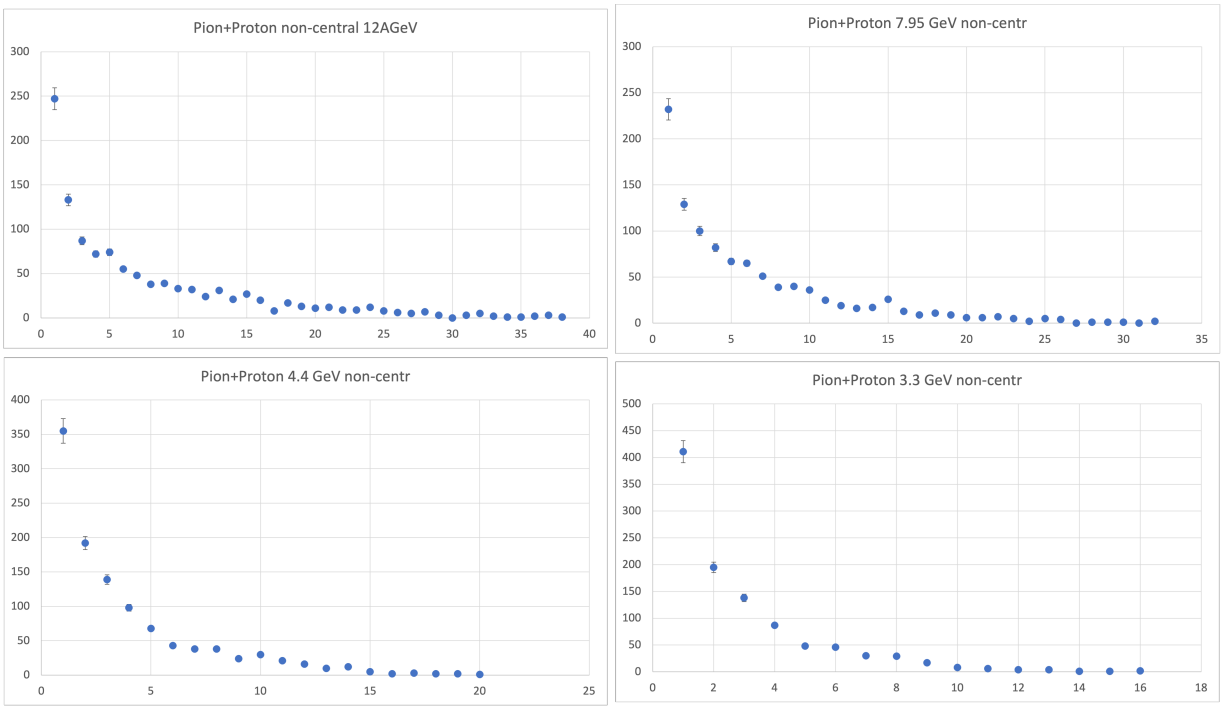

Figure 6.27: A distribution of number of π^+p particle pairs in the first 10 bins for 12 [AGeV/c], 7.95 [AGeV/c], 4.4 [AGeV/c] and 3.3 [AGeV/c], non-central collisions.

Table 6.23: Mean number of π^+p particle pairs in the first 10 bins with standard deviation σ for 12 [AGeV/c], 7.95 [AGeV/c, 4.4AGeV/c and 3.3 AGeV/c, non-central collisions.

π^+p non-central				
	12 [AGeV/c]	7,95 [AGeV/c]	4,4 [AGeV/c]	3,3 [AGeV/c]
mean	4,453	3,905	2,676	2,156
σ	7,475	5,742	3,496	2,542

Table 6.24: The established number of events needed to obtain the statistical error bar of 10%, 5% and 1% for π^+p correlation function for 12 [AGeV/c], 7.95 [AGeV/c], 4.4 [AGeV/c] and 3.3 [AGeV/c], non-central collisions.

π^+p non-central				
	12 [AGeV/c]	7,95 [AGeV/c]	4,4 [AGeV/c]	3,3 [AGeV/c]
10%	225	257	374	464
5%	899	1 025	1 495	1 856
1%	22 454	25 607	37 373	46 380

6.3.2 Establishing needed statistics by analysis of first bin of correlation function

This next method of estimation of the necessary statistics to obtain systematic error of given value of 10%, 5% and 1% is based on analysing the value and the error of the first bin of the correlation function. For this method the whole available statistics (48 million of UrQMD $Au - Au$ collisions, for 4 beam momentum values) was used.

By analysing the first bin of the obtained correlation function one can obtain the value and the error and then, by transforming the formula 6.3, obtain the information about the number of needed events.

$$E_{syst} = \frac{\textit{error of the bin}}{\textit{value of the bin}} \cdot \frac{1}{\sqrt{N}} \tag{6.3}$$

,where E_{syst} is the value of the systematic error one want to obtain ($0,1$ for 10%, $0,05$ for 5%, $0,01$ for 1%) and N is the value of needed statistics.

The estimated number of events needed to obtain the systematic error of order of 10%, 5% or 1% for $p\kappa^+$, $\pi^+\kappa^+$ and π^+p correlation functions, for central and non-central $Au - Au$ collisions for $12[AGeV/c]$, $7.95[AGeV/c]$, $4.4[AGeV/c]$ and $3.3[AGeV/c]$ beam momentum were presented in the Tab.6.25.

The estimated number of events needed to obtain the systematic error of order of 10%, 5% or 1% for $p\kappa^-$, $\pi^-\kappa^+$ and π^-p correlation functions, for central and non-central $Au - Au$ collisions for $12[AGeV/c]$, $7.95[AGeV/c]$, $4.4[AGeV/c]$ and $3.3[AGeV/c]$ beam momentum were presented in the Tab.6.26.

Table 6.25: The established number of events needed to obtain the statistical error bar of 10%, 5% and 1%, by using the method of analysing the first bin of correlation function, for π^+p, κ^+p and $\pi^+\kappa^+$ correlation functions, for 12 [AGeV/c], 7.95 [AGeV/c], 4.4 [AGeV/c] and 3.3 [AGeV/c], central and non-central collisions.

κ^+p central				
	12 [AGeV/c]	7,95 [AGeV/c]	4,4 [AGeV/c]	3,3 [AGeV/c]
10%	1 175 807	1 020 212	664 368	446 327
5%	4 703 225	4 080 848	2 657 470	1 785 308
1%	117 580 623	102 021 187	66 436 729	44 632 681

κ^+p non-central				
	12 [AGeV/c]	7,95 [AGeV/c]	4,4 [AGeV/c]	3,3 [AGeV/c]
10%	1 520 116	1 333 751	877 600	586 722
5%	6 080 461	5 335 002	3 510 397	2 346 886
1%	152 011 520	133 375 029	87 759 916	58 672 127

$\pi^+\kappa^+$ central				
	12 [AGeV/c]	7,95 [AGeV/c]	4,4 [AGeV/c]	3,3 [AGeV/c]
10%	920 624	669 076	310 024	164 101
5%	3 682 496	2 676 303	1 240 093	656 403
1%	92 062 381	66 907 566	31 002 306	16 410 060

$\pi^+\kappa^+$ non-central				
	12 [AGeV/c]	7,95 [AGeV/c]	4,4 [AGeV/c]	3,3 [AGeV/c]
10%	1 231 505	904 426	419 361	216 780
5%	4 926 020	3 617 702	1 677 444	867 120
1%	123 150 481	90 442 538	41 936 087	21 677 998

π^+p central				
	12 [AGeV/c]	7,95 [AGeV/c]	4,4 [AGeV/c]	3,3 [AGeV/c]
10%	2 600 634	2 243 842	1 561 589	1 198 168
5%	10 402 534	8 975 367	6 246 354	4 792 670
1%	260 063 375	224 384 160	156 158 832	119 816 732

π^+p non-central				
	12 [AGeV/c]	7,95 [AGeV/c]	4,4 [AGeV/c]	3,3 [AGeV/c]
10%	3 378 118	2 945 540	2 071 559	1 593 749
5%	13 512 469	11 782 157	8 286 236	6 374 996
1%	337 811 714	294 553 913	207 155 888	159 374 894

Table 6.26: The established number of events needed to obtain the statistical error bar of 10%, 5% and 1%, by using the method of analysing the first bin of correlation function, for $\pi^- p$, $\kappa^- p$ and $\pi^+ - \kappa^+$ correlation functions, for 12 [AGeV/c], 7.95 [AGeV/c], 4.4 [AGeV/c] and 3.3 [AGeV/c], central and non-central collisions.

$\kappa^- p$ central				
	12 [AGeV/c]	7,95 [AGeV/c]	4,4 [AGeV/c]	3,3 [AGeV/c]
10%	550 276	400 062	176 323	87 928
5%	2 201 103	1 600 248	705 289	351 711
1%	55 027 559	40 006 196	17 632 219	8 792 761
$\kappa^- p$ non-central				
	12 [AGeV/c]	7,95 [AGeV/c]	4,4 [AGeV/c]	3,3 [AGeV/c]
10%	748 057	547 273	234 096	113 681
5%	2 992 227	2 189 092	936 383	454 724
1%	74 805 659	54 727 286	23 409 563	11 368 095
$\pi^- \kappa^+$ central				
	12 [AGeV/c]	7,95 [AGeV/c]	4,4 [AGeV/c]	3,3 [AGeV/c]
10%	989 966	734 561	357 832	197 091
5%	3 959 862	2 938 242	1 431 326	788 362
1%	98 996 532	73 456 050	35 783 149	19 709 048
$\pi^- \kappa^+$ non-central				
	12 [AGeV/c]	7,95 [AGeV/c]	4,4 [AGeV/c]	3,3 [AGeV/c]
10%	1 329 107	997 949	487 999	262 614
5%	5 316 428	3 991 796	1 951 994	1 050 453
1%	132 910 694	99 794 900	48 799 842	26 261 309
$\pi^- p$ central				
	12 [AGeV/c]	7,95 [AGeV/c]	4,4 [AGeV/c]	3,3 [AGeV/c]
10%	3 060 056	2 679 562	1 945 233	1 545 357
5%	12 240 224	10 718 248	7 780 930	6 181 425
1%	306 005 577	267 956 180	194 523 240	154 535 617
$\pi^- p$ non-central				
	12 [AGeV/c]	7,95 [AGeV/c]	4,4 [AGeV/c]	3,3 [AGeV/c]
10%	4 101 323	3 648 115	2 689 846	2 136 473
5%	16 405 292	14 592 460	10 759 383	8 545 892
1%	410 132 289	2364 811 496	268 984 570	213 647 279

7. Discussion and summary

This thesis contains the analysis of simulated data for $Au - Au$ collisions at four beam momentum values: $12[AGeV/c]$, $7.95[AGeV/c]$, $4.4[AGeV/c]$ and $3.3[AGeV/c]$, for two centrality intervals: $0 - 10\%$ (central collisions) and $10 - 100\%$ (non-central collisions). Analysis were carried out for p, $\overline{p}$, π^+, π^-, κ^+, κ^-, Λ and $\overline{\Lambda}$ particles.

The first part of the study shown in this thesis consists of the p_T and y ranges that were used in the following analysis and distributions of the basic physical variables used to describe heavy-ion collisions: the four-position vector of the particles $[x, y, z, t]$, the four-momentum vector $[p_x, p_y, p_z, E]$ and p_T, r_T, y, η, for 100 000 $Au - Au$ central and non-central collisions, for $12[AGeV/c]$ beam momentum.

The next part of the work describes the analysis of the $\pi^-\pi^-$ and $\kappa^+\kappa^+$ correlations in order to obtain the source size of the emitted particles by parametrization of the correlations functions. Those studies were performed for four beam momentum values: $12[AGeV/c]$, $7.95[AGeV/c]$, $4.4[AGeV/c]$ and $3.3[AGeV/c]$, for two centrality intervals: $0 - 10\%$ (central collisions) and $10 - 100\%$ (non-central collisions) and for four k_T ranges: $(0.15; 0.25)$, $(0.25; 0.35)$, $(0.35; 0.45)$ and $(0.45; 0.60)[GeV/c]$. Based on the obtained results, it can be stated that the size of the source has the highest value for the central collisions and decreases for the peripheral ones. It can also be noticed that the values of the size of the source decreases as the value of beam momentum gets lower and it also decreases for higher k_T. The obtained sizes of the source are in the range from $5.370[fm]$ to $4.720[fm]$ for $\pi^-\pi^-$ correlations and from $3.170[fm]$ to $2.830[fm]$ for $\kappa^+\kappa^+$ correlations. Source sizes obtained for the $\pi^-\pi^-$ particle pair correlation can be compared with the results from the Alternating Gradient Synchrotron (AGS) in Brookhaven [25] for beam energies values close to the beam energies used in this study. The results are similar.

Finally, the last part of the results shows the analysis conducted to estimate the required number of $Au - Au$ collisions needed to obtain correlation functions with systematic error of 10%, 5% and 1% for the p, κ and π particle pairs, for two ranges of centrality and four

values of beam momentum: $12[AGeV/c]$, $7.95[AGeV/c]$, $4.4[AGeV/c]$ and $3.3[AGeV/c]$, for UrQMD data. The estimation of the necessary statistics was done by using two methods.

The first method is based on analysing correlation function in the area of k^* where the correlation effect occurs. Then, p, π and κ particles pairs correlation functions were created in the established region of k^* with just 10 bins, which were later analyzed. In the second method, the first bin of the correlation function was studied. This calculations required the use of the whole gathered data (48 million events). This method, as it is much quicker than the first one, allowed to analyse the unlike-sign particle pairs.

It can be easily noticed that for both methods the required number of collisions is much higher for non-central collisions than for the central ones. For the first method, the required number of requires $Au - Au$ collisions is decreasing with the increase of the beam momentum values. For the second method however, the required number of collisions is increasing with the increase of the beam momentum values. Moreover, the basic dependence is visible - the lover is the value of the desired systematic error, the higher is the required number of $Au - Au$ collisions. Additionally, for the unlike-sign particle pairs studied in the second method, the statistics is higher than for like-sign particle pairs. It can be a result of the low multiplicity of the negatively charged particles.

When comparing the two methods, it can be stated that the second method of establishing statistics by analysis of the first bin of the correlation function is much faster than the first method, where the required number of collisions is established by analyzing the first 10 bins of the correlation function.

The difference between the statistics first and the second method is of order of 10^3 events for $12[AGeV/c]$ and $7.95[AGeV/c]$ beam momentum and of order of 10^2 for $4.4[AGeV/c]$ and $3.3[AGeV/c]$ beam momentum. For π^+p particle pair the difference is even bigger and is of order of 10^4 events for $12[AGeV/c]$ and $7.95[AGeV/c]$ beam momentum and of order of 10^3 for $4.4[AGeV/c]$ and $3.3[AGeV/c]$ beam momentum.

This huge discrepancy in obtained number of statistics can be the result of the difference in the number of analyzed data. In the first method, the used sample was small, it contained only 1000 events. Besides that, this method studied only the events in which the studied particle pairs could be found. The second method based on the analysis of the 48 million events and studied all of them.

When taken those differences into the consideration it could be understood that the first method requires more steps and has to be further developed to obtain the results similar to the second method, which is much quicker, as it allowed to analyse the unlike-sign particle pairs.

The aim of the study was to gain information about nonidentical particle pairs correlation functions in Monte Carlo simulations for the CBM experiment at FAIR. The obtained results are helping to prepare for the work which will be done after the launch of the CBM experiment in the 2025.

A. Appendix A

Table A.1: An example of input file for UrQMD simulation of data.

```
# projectile and target Au, Au
pro 197 79
tar 197 79
# number of events
nev 10000
# impact parameter, for central collisions (0;3.2)
#for non-central (3.2;15.0)
IMP 0.0 3.2
cto 5 1
cto 44 0
# beam momentum AGeV
plb 12.0
tim 200 200
eos 0
# seed
rsd 12345
# suppress output to .f19 file:
f13
f14
f15
f16
#f19
f20
xxx
```

B. Appendix B

Table B.1: An example of code from NicaFemto for obtaining correlation functions for non-identical particle pairs.

```
NicaFemtoBasicAna *ana = new NicaFemtoBasicAna();

        NicaFemtoCorrFuncKt kt(NicaFemto1DCF("kt",100,-0.25,0.25,
        ENicaFemtoKinematics::kPRF), {0.1,2.0});
        ana->SetPdg(211,321);
        ana->SetCorrFctn(kt);
        ana->SetOption(NicaTwoTrackAna::BackgroundOptionMixed());
        ana->EnableNonIdentical();

        NicaTrackBasicMCCut track_cut;
        track_cut.SetPdgCut(PID);
        track_cut.SetPtCut(0.2,1.0);
        track_cut.SetEtaCut(-2.0,2.0);
        ana->AddCut(track_cut);

        NicaTrackBasicMCCut track_cut2;
        track_cut2.SetPdgCut(PID2);
        track_cut2.SetPtCut(0.2,1.5);
        track_cut2.SetEtaCut(-2.0,2.0);
        ana->AddCut(track_cut2);


        NicaEventImpactParameterCut event_cut;
        event_cut.SetMinMax(0.0,3.2);
        ana->AddCut(event_cut);
```

```
        track_cut.Pt(),track_cut.CutName(), 3);
        ciecie.SetXaxis(100,0,2);
        ciecie.SetYaxis(100,-2,2);

        NicaCutMonitorX hassan(event_cut.CutName());
        hassan.SetXaxis(100,0,15.0);
        ana->AddCutMonitor(hassan);

        ana->SetFormat(new NicaUnigenEvent());
        ana->AddCutMonitor(ciecie);
        return ana;
}

void simple_hbt1d_centr_1_00001(TString inFile = "/lustre/nyx/cbm
/users/wborzym/production/auau_12/test_00001.root",
TString outFile = "/lustre/nyx/cbm/users/wborzym/cf/1.root"){
        FairRunAna *fRun = new FairRunAna();
        fRun->SetEventHeaderPersistence(kFALSE);
        fRun->SetSource(new NicaUnigenSource(inFile));
        fRun->SetOutputFile(outFile);

        NicaFemtoWeightGeneratorLednicky calc;
        calc.SetPairType(ENicaFemtoPairType::kPionPlusKaonPlus);
            calc.SetQuantumOff();
            calc.SetCoulOn();
            calc.SetStrongOn();
        NicaFemtoWeightGeneratorBasic calc_basic;

        NicaFemtoBasicAna *ana1 = fun(211,321);

        ana1->SetWeight(calc);
        fRun->AddTask(ana1);

        fRun->Init();
        fRun->Run(0,10000);
}
```

List of Figures

List of Tables

Bibliography

[1] Donald H. Perkins. *Introduction to High Energy Physics*. Cambridge University Press, 2000.

[2] Wikimedia Commons. *File:Standard Model of Elementary Particles.svg — Wikimedia Commons, the free media repository*. https://commons.wikimedia.org/w/index.php?title=File:Standard_Model_of_Elementary_Particles.svg&oldid=609231940. [Online; accessed 9-August-2021]. 2021.

[3] H. P. Zbroszczyk. "Eksperymentalne aspekty badania korelacji femtoskopowych w zderzeniach relatywistycznych ciężkich jonów". In: *Prace Naukowe Politechniki Warszawskiej. Fizyka* z. 59 (2018), 3–260. ISSN: 1643-6857.

[4] *The official site of Katarzyna Grabieszkow for lecture on "Heavy Ion Physics"*. http://www.if.pw.edu.pl/~kperl/. Accessed: 2021-08-19.

[5] Mikhail Stephanov. "QCD phase diagram and the critical point". In: *Progress of Theoretical Physics Supplement* 153 (2004), pp. 139–156.

[6] *Hanna Zbroszczyk - private correspondence*.

[7] Raimond Snellings. "Elliptic flow: a brief review". In: *New Journal of Physics* 13.5 (2011), p. 055008. DOI: 10.1088/1367-2630/13/5/055008.

[8] Hanna Paulina Zbroszczyk. *Eksperymentalne aspekty badania korelacji femtoskopowych w zderzeniach relatywistycznych ciezkich jonów*. Oficyna Wydawnicza Politechniki Warszawskiej, 2019.

[9] S. K. Tiwari and C. P. Singh. "Particle Production in Ultrarelativistic Heavy-Ion Collisions: A Statistical-Thermal Model Review". In: *Advances in High Energy Physics* 2013 (2013), 1–27. ISSN: 1687-7365. DOI: 10.1155/2013/805413.

[10] Odyniec Grażyna. *Quark Matter and the journey to the beginning of the Universe*. The series of lectures on the Faculty of Physics at Warsaw University of Technology.

[11] *Explanation of the azimutal angle*. https://www.quora.com/What-is-meant-by-the-azimuthal-angle. [Online; accessed 15-August-2021].

[12] Monika Seniut. “Therminator generator adaptation to the conditions of RHIC and FAIR experimental complexes”. PhD thesis. 2017.

[13] Sebastian Siejka. “Budowa systemu informatycznego do wyznaczania dwucząstkowych rozkładów pędowych w ramach eksperymentu STAR przy użyciu modeli teoretycznych”. PhD thesis. 2014.

[14] Daniel Wielanek. “Feasibility of the femtoscopic measurements in CBM experiment”. In: *36th CBM Collaboration Meeting* (2020).

[15] Zbroszczyk Hanna. “Studies of baryon-baryon correlations in relativistic nuclear collisions registered at the STAR experiment”. PhD thesis. 2008.

[16] Adam Kisiel. “Studies of non-identical meson-meson correlation at low relative velocities in relativistic heavy-ion collisions registered in the STAR experiment”. In: *Warsaw University of Technology* (2004).

[17] Paweł Szymański (for the STAR collaboration. “Non-identical particle femtoscopy at STAR”. In: *XIII Workshop on Particle Correlation and Femtoscopy Cracow, 22.05.18* (2018).

[18] J. Knoll S. Leupold J. Randrup R. Rapp P. Senger B. Friman C. Höhne. *The CBM Physics Book Compressed Baryonic Matter in Laboratory Experiments*. Springer, 2011.

[19] *The official site of Facility for Antiproton and Ion Research*. https://fair-center.eu/overview/accelerator. Accessed: 2021-08-30.

[20] Volker Friese. “The high-rate data challenge: computing for the CBM experiment”. In: *Journal of Physics: Conference Series* 898 (Oct. 2017), p. 112003. DOI: 10.1088/1742-6596/898/11/112003.

[21] Evgeny Lavrik. “Development of quality assurance procedures and methods for the CBM Silicon Tracking System”. PhD thesis. Nov. 2017. DOI: 10.15496/publikation-20433.

[22] *The official site of UrQMD collaboration*. https://urqmd.org/. Accessed: 2021-08-22.

[23] *NicaFemto repository*. https://git.jinr.ru/Wielanek/nicafemto. Accessed: 2021-08-30.

[24] Daniel Wielanek et al. “Femtoscopy Studies at NICA Energy Scale”. In: *Acta Physica Polonica B Proceedings Supplement* 9 (Jan. 2016), p. 341. DOI: 10.5506/APhysPolBSupp.9.341.

[25] M. A. Lisa et al. “Bombarding Energy Dependence of π^- Interferometry at the Brookhaven AGS”. In: *Phys. Rev. Lett.* 84 (13 2000), pp. 2798–2802. DOI: 10.1103/PhysRevLett.84.2798. URL: https://link.aps.org/doi/10.1103/PhysRevLett.84.2798.